Prototyping a High Frequency Inductive Magnetic Sensor Using the Non-Conventional, Low Temperature Co-Fired Ceramic Technology for Use in ITER

D.Testa[1], Y.Fournier[2], T.Maeder[2], M.Toussaint[1], R.Chavan[1], J.Guterl[1], J.B.Lister[1], J-M.Moret[1], B.Schaller[1], G.Tonetti[1]

[1] Centre de Recherches en Physique des Plasmas, Ecole Polytechnique Fédérale de Lausanne (CRPP–EPFL), Association EURATOM – Confédération Suisse, CH–1015 Lausanne, Switzerland

[2] Laboratoire de Production Microtechnique, Ecole Polytechnique Fédérale de Lausanne (LPM – EPFL), CH-1015 Lausanne, Switzerland

e-mail address of contact author: duccio.testa@epfl.ch

Galley proofs are to be sent to:

Duccio Testa, Centre de Recherches en Physique des Plasmas, Ecole Polytechnique Fédérale de Lausanne, Station 13, CH–1015 Lausanne, Switzerland

Tel: +41-216933568, Fax: +41-216935176, e-mail: duccio.testa@epfl.ch

Total number of pages: 28 (excluding 1st page, captions, Tables and Figures)

Total number of separate Tables (if TableX is split in TableX-a and TableX-b, it counts as 2): 3

Total number of separate Figures (if figX is split in figX-a and figX-b, it count as 2): 24

Figures to be printed in color: none

Figures to be printed in black/white: all

Prototyping a High Frequency Inductive Magnetic Sensor Using the Non-Conventional, Low Temperature Co-Fired Ceramic Technology for Use in ITER

D.Testa, Y.Fournier, T.Maeder, M.Toussaint, R.Chavan, J.Guterl, J.B.Lister, J-M.Moret, B.Schaller, G.Tonetti

Abstract

The ITER high-frequency (HF) magnetic sensor is currently intended to be a conventional, Mirnov-type, pick-up coil, designed to provide measurements of magnetic instabilities with magnitude as low as $|\delta B| \sim 10^{-4}$G at the position of the sensors, and up to frequencies of at least 300kHz. Previous prototyping of this sensor has indicated that a number of problems exist with this conventional design, which are essentially related to the winding process and the differential thermal expansion between the metallic wire and the ceramic spacers. Hence, a non-conventional HF magnetic sensor has been designed and prototyped in-house in different variants using the Low-Temperature Co-fired Ceramic (LTCC) technology, involving a series of stacked ceramic substrates with a circuit board printed on them with a metallic ink (silver in our case). A method has then been developed to characterize the electrical properties of these sensors from the DC range up to frequencies in excess of 10MHz. This method has been successfully benchmarked against the measurements for the built sensors, and allows predicting with confidence the electrical properties of LTCC prototypes without the need of actually building them, therefore significantly simplifying future R&D activities. When appropriate design choices are made, LTCC sensors are found to meet in full the volume occupation constraints and the requirements for the sensor's electrical properties which are set out for the ITER HF magnetic diagnostic system. This non-conventional technology is therefore recommended for further R&D and prototyping work, particularly for a 3D sensor, and possibly using materials more suitable for use in the ITER environment, such as palladium and platinum inks, which could remove the perceived risk of transmutation under a heavy neutron flux that we may have with the Au (to Hg, then to Pb) or the Ag (to Cd) metallic inks currently used in LTCC devices.

(I) Introduction

The ITER high frequency (HF) magnetic sensor is currently intended to be a conventional, Mirnov-type, pick-up coil, i.e. a metallic (tungsten) wire wound around a ceramic insulating former, so as to have an effective area $(NA)_{EFF}$ of the order of $(NA)_{EFF}\sim(0.05\div0.10)m^2$. This sensor is designed to provide measurements of magnetic instabilities with magnitude as low as $|\delta B|\sim10^{-4}G$ at the position of the sensors, and up to frequencies of at least 300kHz. This pick-up coil is currently intended to be made with 33 turns each on 2 separate layers, wound over a hollow hexagonal ceramic body. This body can be manufactured as a single component to have a much stronger part, on which sections are effectively "carved-out" using some machining (or molding) processes, so that these sections will in fact act as individual wire spacers, or as a set of individual thin disks, easier to manufacture but individually weaker and requiring additional fixings to be kept in position during the assembly of the coil. A stainless steel core mechanically supports the insulating former, and improves thermal conduction. The coil is then fixed onto a metal plate that allows thermal and electrical contact with the ITER vacuum vessel. The sensor's design parameters (effective area, electrical properties), are intended to be such that a signal exceeding at least $V_{MEAS}>50mV$ (i.e. at least twice above what is estimated to be the intrinsic bit-noise level) should be obtained at the front-end electronics (which will be located not closer than 50m away from the detector), this even at the lower frequencies in the measurements (currently intended to be between 1kHz and 10kHz, depending on a possible use of these sensors as backup measurements for equilibrium reconstruction). Finally, when integrating the different and continuously evolving ITER measurement requirements for HF instabilities[1, 2], this diagnostic system must have the capability of recognizing toroidal mode numbers (n) at least up to $|n|=30$ and poloidal mode numbers (m) up to $|m|=60$ in all the main ITER operating scenarios. To this end, a system layout with between 170 and 500 individual sensors is being proposed [3].

The Mirnov-type design for this sensor was prototyped in different variants [4, 5], and this work has demonstrated that this conventional design is not suitable for the manufacturing of an HF magnetic sensor for ITER, essentially because of the differential thermal expansion between the wires and the

ceramic spacers and too high a risk of breakages during the assembly of the winding pack. These previous prototyping results have motivated a search for alternative manufacturing methods for the ITER HF magnetic sensors, and two options were considered: a laser-cut non-conventional, but still Mirnov-type, pick-up coil, the prototyping of which is also reported in [4 ,5], and a completely new approach in the ITER framework, i.e. the Low-Temperature Co-fired Ceramic (LTCC) technology. This technology provide a good starting point, as it is already an industry standard widely used for high temperature and high vacuum applications. Moreover, the very similar HTCC standard (High-Temperature) has been previously used for the manufacturing of 3D inductive magnetic sensors for use in LHD [6] (note that one spare sensor of the batch described in [6] was also later installed in NSTX for comparison purposes with the usual Mirnov-type sensors [7]). Some design studies with HTCC sensors were also performed for MAST, but were not pursued because of high R&D costs and the technical difficulties associated with using sensors with high self-resistance [8]. Finally, the LTCC technology is also being considered for the low-frequency discrete magnetic sensors to be used in ITER for the in-vessel measurements of flux and fields for equilibrium reconstruction [9].

Even if the first examples were produced in the late nineties using the HTCC technology, ceramic encapsulated inductive magnetic sensors are currently not a usual measurement device for magnetic fluctuations in fusion experiments, conventional Mirnov-type coils being the norm, the main reason being the rather high R&D costs for the design and production of such sensors when this work is done in collaboration with commercial firms. This is not a problem for our academic institution, as we have an in-house facility for manufacturing such LTCC and HTCC devices. The main difference between the HTCC and LTCC technologies resides in the firing temperature, about ~1450°C for the former vs. ~900°C for the latter, allowing the use of lower-resistivity materials (such as gold and silver) as a conducting ink in LTCC devices. Conversely, the higher firing temperature and lower thermal conductivity of HTCC devices allows using stronger materials for the ceramic substrate, such as alumina (Al_2O_3), which in principles allows producing more robust 3D structures more easily; hence the assembly has a much higher mechanical rigidity and hermeticity, which are important factors for the environmentally demanding applications of the aeronautical, automotive

and nuclear industries. Table1 gives a summary of the main electrical and thermal properties of the metallic inks used for HTCC and LTCC devices. The HTCC metallic inks (molybdenum, tungsten), have a slightly higher magnetic susceptibility, a lower thermal conductivity but a higher resistivity, with a higher temperature coefficient, which in turns increases the self-heating of the sensor and its temperature-induced voltage drifts. Since our experience is that inductive magnetic sensors with the higher self-resistance (and a higher temperature coefficient of resistivity) are the more affected by electrical pick-up, hence requiring a more complex scheme for the grounding, cabling, common mode rejection and load resistance termination at the input of the front-end electronics to mitigate such effect, LTCC devices are in our view a more practical choice than HTCC ones when explicitly considering the environmental constraints (nuclear and radiation heating, risk management) [2, 10] and the measurement requirements for the HF magnetic instabilities in ITER [1, 2].

Our LTCC prototyping work has focused for the time being on 1D sensors and has been performed around four main stages. First, we have designed and produced in house a number of sensors with systematic variations in various design features around a baseline design to assess the effect of these design options on the frequency response of the sensors. Second, we have measured the impedance of these sensors to extract their electrical properties, specifically the self-inductance, self-resonance frequency, quality factor and effective area. Third, these electrical data have been analyzed using a previously developed method [4] to develop the equivalent circuit model for the sensors. Finally, the success of this validation exercise has allowed us to produce scaling laws for the main electrical properties of the LTCC sensors, so that future prototypes can be designed and built with much greater confidence in their predicted frequency response, clearly facilitating future R&D activities.

This paper is organized as follows. Section II presents the design and the in-house manufacturing of the prototype LTCC sensors. Section III presents the measurements and Section IV the analysis of the main electrical characteristics (self-inductance, self-capacitance, self-resistance, self-resonance frequency, bandwidth, quality factor and effective area) of these prototypes. Section V describes the modeling results for the scaling to future prototypes. Finally, in Section VI we give a summary and present the conclusions of this work, and Section VII presents an outlook towards future activities.

(II) Design choices and manufacturing of the prototype HF LTCC magnetic sensors

A ceramic encapsulated sensor is built up from thin ceramic tapes, with thickness ~(100÷400)μm (when unfired), onto which an appropriate metallic ink is screen printed to form windings and to ensure interlayer electrical connection through "*via*" holes. Figure1 shows the main manufacturing steps of the LTCC substrate production, starting with the unfired ceramic base, the so-called "*green sheets*". The manufacturing of the *green sheets* ensures maximum flexibility, especially with respect to the mechanical properties of the substrates. After cutting the sheets to the desired size, the holes for the *vias* and cavity openings are mechanically punched. The next step is filling the *vias* with a conducting paste. The paste is applied through a mask with openings at the positions of the *vias*. Standard diameters for the *vias* range from 100μm to 200μm, depending on tape thickness. Then, the conducting traces are screen-printed: the minimum line width and the minimum line separation are 60μm each. The ceramic tapes are then stacked on top of each other, possibly intercalated with additional tapes carrying no winding planes (just *vias* to ensure the electrical connection between the layers) to decrease the interlayer capacitance (a so-called "*neutral layer*"). Afterwards, the tapes are laminated iso-statically in a pressurized tank or uni-axially at temperatures around 70°C. The final step is the firing in air at temperatures of up to ~875°C for the LTCC and ~1450°C for the HTCC standards, respectively. The fired material shrinks by approximately 12.5% in the plane of each ceramic substrate (the xy-plane), and by approximately 15% across the stacked-up spiral layers (the z-axis). The highly homogeneous structure of the *green sheets* and precise temperature control during the firing process ensure dimensional accuracy and high reproducibility. This then allows the realization of cavities for mounting semiconductor chips. These ceramic-encapsulated sensors then very much resemble the conventional Mirnov-type pick-up coils, i.e. a solenoid-like winding with NN spiral layers along the solenoid z-axis (the direction of the stacked-up ceramic substrates) and MM turns across the perpendicular xy-plane (i.e. the plane of each individual ceramic substrate).

The HTCC and LTCC technologies have become industrial standards for high-reliability electronics subject to harsh environmental conditions, such as high-temperature and high-vacuum applications

in the automotive, aeronautical and nuclear energy sectors; hence, industrial production of LTCC and HTCC devices has become commonplace and achieves a very high reproducibility. Considering now the particular case of inductive magnetic sensors for thermonuclear fusion experiments, and comparing the ceramic encapsulated with the conventional Mirnov-type design, the great advantage of the former is its much smaller and compact size, significantly simplifying the volume occupation constraints for in-vessel installation and making it possible to design and manufacture a 3D sensor using only a fraction of the volume needed for 3× 1D conventional pick-up coils, as demonstrated by the previous work using the HTCC technology [6]. Moreover, ceramic encapsulated sensors do not require the complex handling operations needed to assemble the *winding pack* in Mirnov-type sensors. Finally, as the conducting traces are fully buried within the ceramic substrates after the lamination and firing, there is no separate winding as such, hence there is no differential expansion due to a thermal mismatch between the winding and the ceramic support, and the *winding pack*[♦] is completely screened from the external environment. The remaining issue for ceramic encapsulated sensors is related to the output winding terminations, as these will be electrically connected to the in-vessel wiring, which will be made using a different conducting material (for instance a mineral insulated cable with a Glidcop core). The connections can still be fully insulated using (fiber-)glass encapsulation, but there would still be some unavoidable thermal EMF (via the Peltier effect), which is however currently estimated to be very minor (<5mV for a full-length ITER plasma pulse). The main drawback of the LTCC technology is related to the metallic ink used to screen-print the circuit, as current manufacturing processes (not only in-house but also those industrially available) use conductive inks based on gold and silver, whereas such inks may have to be avoided in ITER due to a perceived risk of (however small) transmutation to cadmium (Ag→Cd), mercury and lead (Au→Hg→Pb) under the expected neutron and radiation fluxes. Using inks such as palladium or platinum is thought to remove these risks of transmutation, but LTCC manufacturing processes for these inks are currently not well established. However, it is intuitively expected that, as an alloy is

♦ Note that we use the term “winding pack” for ceramic encapsulated magnetic sensors as it is usually referenced in the more familiar framework of wire-wound magnetic sensors, i.e. the winding pack is the ensemble of all the individual turns on all the individual layers that make up the whole of the sensor.

formed when sintering an LTCC sensor, the metallic ink will be fully buried, hence sealed, within the surrounding *green tape*. Therefore, there would be essentially no Cd and Hg (or Pb) out-gassing from the LTCC structures, as any such atoms would attach to, hence remain confined within, the structural imperfections of the metallic tracks [11]. The sensor-wiring electrical connections can also be sealed by applying a vacuum-compatible ceramic paste or using (fiber-)glass encapsulation after bonding, further reducing the risk of such out-gassing.

A second drawback is related to the stacking up of a large number of layers in LTCC devices, as it is thought that it becomes more difficult to guarantee the electrical continuity through the *vias* as the number of layers increases, particularly for 3D structures. For instance, we understand from our discussions with various European manufacturers of ceramic encapsulated devices that the current industrial processes are generally developed for large-scale production only up ~10 layers. In our in-house facility, we have been able to laminate and fire LTCC sensors with up to 20 layers, even if with somewhat greater difficulties and requiring a slightly longer production time than when using the standard 10 layers setup. Specifically, for the 1D LTCC sensors we have produced, we have had no problem with the electrical continuity through the limited number of *vias* (~50-200 depending on the sensor), the only cause of electrical fault in the sensors being the presence of very minute particles of dust in our university-standard clean room (confirmed by 3D X-ray tomography of the faulty sensors), which can then attach to the unfired layers as they might have built up some static electricity while resting in the laboratory before lamination.

The essential goal of the prototyping tests on the ITER HF magnetic sensors is to be able to produce a design for a device which is going to be sufficiently strong, easy to manufacture by conventional processes, easy to assemble and mount on its in-vessel support structure and, finally, fully satisfying the ITER measurement requirements for HF magnetic instabilities. Starting from our operational experience acquired on the JET and TCV tokamaks, and when considering explicitly the estimated length (>50m) and the specifications currently available for the electrical characteristics of the in- and ex-vessel signal cables up to the front-end electronics and the data acquisition modules in ITER [12], it is clear that the ITER measurement requirements for HF magnetic instabilities translate into

the sensors having an effective area $(NA)_{EFF}>0.05m^2$, a self-resonance frequency $\omega_0>2\pi\times5MHz$ with a self-inductance $L_{SELF}<100\mu H$, and a quality factor Q less than 30, Q being the ratio between the coil's self-resonance frequency and its bandwidth (γ). A lower quality factor for the coil's self resonance (i.e.: a larger bandwidth) in fact means that the variation in the sensor's impedance for frequencies around the self-resonance is smoother than if the resonance is very sharp, which in turns implies that the resonance band can be resolved correctly and its effect more easily calibrated out from the raw data measurements.

Putting our work into historical perspective and comparing the ITER requirements for the sensors' electrical properties with those obtained in Ref.[6], we note that the HF HTCC sensors installed in LHD have a very low self-inductance $L_{SELF}\sim(0.8\div2.5)\mu H$, which is a very desirable feature for such magnetic sensors, but also have a very low effective area $(NA)_{EFF}\sim(0.12\div0.15)\times10^{-2}m^2$, which on the other hand reduces significantly the sensitivity of the sensors. Our original development work is therefore aimed at achieving $(NA)_{EFF}>0.05m^2$ while keeping as low as possible both L_{SELF} and the sensor's self-capacitance C_{SELF}. Note that since the electrical characteristics of the in- and ex-vessel cabling for the HF magnetic sensors in ITER have not yet been formally finalized (as this wiring is the subject of ongoing R&D work), it is in fact not possible to use the simple understanding that the only important sensor' electrical parameter is the self-inductance, because it is now not justified to assume that the sensor self-capacitance will be much smaller (i.e. at least a factor 20 lower) than that of the signal cabling, which is the usual case for similar sensors in current fusion experiments. Therefore, the design choices for the LTCC sensor have focused on establishing experimentally the scaling of its electrical properties (self-resistance R_{SELF}, L_{SELF}, C_{SELF}, $(NA)_{EFF}$) vs. the geometry of the sensor, such as the number of turns on each layer, the number of layers and the separation between them.

As our in-house facility has already more than 10 years of experience in producing LTCC devices, the main reason for which we have built and measured directly the electrical properties of these prototypes, instead of simply relying on their numerical calculations, is that we have encountered

many difficulties in calculating C_{SELF} using conventional software packages such as COMSOL [13] and FEMM [14]. This is due to the fact that the value of C_{SELF} which was calculated numerically is a strong function of the meshing used to model the sensor's geometry. This in turns implies that a very fine meshing is needed, which on one end exceeds by far our usual run-time computational resources, and on the other end casts some doubts on the overall accuracy of such calculations, as the meshing size required to achieve a stable solution (i.e. one that does not change any further for even a finer meshing) becomes comparable to the expected size of the manufacturing irregularities of such LTCC sensors. As the sensor's self-capacitance and self-inductance determine the self-resonant frequency, by building different prototypes and performing these measurements directly, we expect to understand how to evaluate empirically these electrical data when the geometrical parameters of the LTCC sensors are changed, and determine experimental scaling laws that we can, in turns, back up with some further theoretical and circuit model understanding. Finally, this would then allow us to simulate more accurately the LTCC sensors and optimize their geometrical design parameters for further manufacturing and prototyping tests.

In order to determine the electrical characteristics of the LTCC sensors (i.e. R_{SELF}, L_{SELF}, C_{SELF} and $(NA)_{EFF}$), more than 20 different variants of 1D prototypes have been designed and built in-house:

a) the number of turns on each layer on the xy-plane was varied as MM=[5, 10, 20];
b) the number of spiral layers along the z-axis was varied as NN=[2, 4, 6, 8, 10];
c) each one of the sensors with MM=[5, 10, 20] turns on NN=4 spiral layers was duplicated by adding a *neutral layer*, therefore doubling the separation between the individual conducting ceramic substrates (hence also doubling the total thickness of the sensor), which is expected to reduce mainly the overall self-capacitance of the sensor;
d) each one of the sensors with MM=20 turns on NN=[4, 6] spiral layers was duplicated by shifting the wiring pattern between the odd and even layers, so as not to have directly super-imposed prints (i.e. using staggered layers, as shown in fig2) and test the effect of this design choice on the sensor's self-inductance and self-capacitance;

e) finally, each individual design was also built in a few (2-4) examples to test the reproducibility of the manufacturing process with respect to the electrical properties of the sensors.

To simplify the in-house manufacturing, we have always used a silver metallic ink on a DuPont951 ceramic substrate: the un-shrunk layer thickness is 220μm (which typically reduces to ~216μm after firing), and the size of the sensor in the xy-plane is (30×30)mm. Depending on the total number of layers and their separation (single or double, i.e. adding one neutral layer in between the conducting ones), the total sensor's thickness along the z-axis is ~(0.7÷2.4)mm. The z-axis thickness of the conductive lines, and their width and separation in the xy-plane are also kept fixed at 10μm, 200μm and 400μm, respectively. In principle we can change these parameters for LTCC devices built in-house, although with more complex production processes, particularly if using other metallic inks (such as gold, platinum or palladium) instead of silver. However, as one of the main focuses of our work is benchmarking a model for evaluating the electrical characteristics of the LTCC sensors, so that we can avoid in future the often tedious exercise (even if not particularly costly when the work is carried out in-house) of making a large number of different prototypes with minor variations between them, these further production tests have been initially left aside for future consideration.

Table2 shows the main electrical and physical properties of the materials (ceramic substrate, silver ink, *vias* filling) used to manufacture in-house these prototypes. As used in the following parts of this paper, each prototype is code-named using the format "MMt(i)NNc(d)(x)", i.e. with its number of turns on the xy-plane "MM" followed by the letter "t", then the number of spiral layers along the z-axis "NN" followed by the letter "c", and finally specifying its (optional) variant using the letters within the brackets. As an example of this format, the code-name "20ti4cd3" indicates the sensor with MM=20 turns, NN=4 spiral layers, with wiring in the odd/even layers not super-imposed (i.e. staggered), as indicated by the bracketed letter (i), using double thickness along the z-axis, as indicated by the bracketed letter (d), this particular sensor also being the 3rd manufactured prototype of its kind, as indicated by the bracketed number (3).

Figure3(a-d) shows the manufacturing drawings for each individual layer of the 1D LTCC prototypes, using the nominal 1-turn geometry (fig3a, top left), and the actual 5-turn (fig3b, top right), 10-turn (fig3c, bottom left) and 20-turn geometries (fig3d, bottom right). Note the difference in the shape of the turns in each plane, particularly in the radius "R" of the quasi-circular corners: the smaller the R, the more complex the screen printing and the more careful the lamination process has to be. The geometrical patterns of the turns are also slightly different across successive layers, to ensure that the electrical connections are made across the z-axis using straight (vertical) conducting *vias*, which are much easier to punch and fill, particularly with many super-imposed layers. Figure4 shows a 3D view of the 5t4cd sensor (5 turns, 4 spiral layers, double-thickness), to illustrate in more details its assembly with the conducting and the *neutral* layers, and the inter-layer connections through filling of the *via* holes. Finally, fig5 shows some of the LTCC prototypes. Note the very small size of these devices ~(3×3×0.2)cm, compared to that of conventional Mirnov-type pick-up coils, ~(10×5×5)cm.

(III) Measurement and calculation of the electrical characteristics of the LTCC sensors

The electrical characteristics of the HF magnetic sensor can be extracted from the measurement of its impedance (Z-data) using the numerical techniques described in details in [15] and Appendix-A of [4], briefly reviewed here for clarity. This technique makes use of our knowledge of the electrical structure of a circuit with an HF magnetic sensor. Basically, we measure the circuit impedance vs. frequency and then use the circuit structure to determine the AC component of the overall transfer function, using then geometrical data or measurements made with an Helmholtz coil to deduce the "DC" gain of the sensor, i.e. its effective area. The AC response curves are in general non-trivial because the probe circuits are non-ideal: the simple response function of an HF magnetic sensor

$V_{MEAS}(\omega) = \left(NA\right)_{EFF}(\omega) \times i\omega \times B_{MEAS}(\omega)$	(1)

describes the voltage induced across the probe by a time-varying magnetic field, but the probe has a finite self-inductance and resistance, and it is connected (in principle) to a long set of cables, each

with its own inductance and capacitance. Circuit resonances therefore alter the voltage that reaches the front-end electronics compared to that measured at the probe itself.

For AC circuits it is convenient to work in the Laplace (s=iω) frequency-domain space. Here the output signal S (in digitizer counts) of the front-end electronics is related to the rate of change of the magnetic field $\partial B_{MEAS}/\partial t$ along the probe axis via (see [15b] for more details):

$S[counts] = H_D(s)[count/V] \times V_{MEAS}(s)[V] = H_D(s) \times H_P(s) \times B_{MEAS}(s),$	(2)

where $H_D(s)$ is the AC transfer function of the data acquisition electronics, $H_P(s)$ is the complete AC transfer function of the probe-cable section, including the term $s \times (NA)_{EFF}(s=0)$, and B_{MEAS} is the magnetic fluctuation being measured at the probe. The two transfer functions $H_D(s)$ and $H_P(s)$ can individually be represented in the frequency domain as H(s)=B(s)/A(s), where B(s) is the output and A(s) is the input. The calibration problem then reduces to the problem of determining $H_D(s)$ and $H_P(s)$. For the case of the HF magnetic sensors studied here, we do not consider the measurement and interpretation of $H_D(s)$ as we analyze the impedance measured at the sensor's output (hence we can assume that $H_D(s)=1$). Furthermore, the probe-cable circuits consist simply of the probe itself plus a very short (<20cm) screened twisted-pair cable that brings the signal from the sensor to the impedance measurement device, in our case an impedance-meter. The simplest circuit model which can reasonably account for the probe's (series) inductance and resistance, but neglects the cable except for its capacitance and admittance (parallel resistance), in parallel with the probe itself, is shown at the top of fig6. This is conceivable since the wavelength of a 1MHz (i.e., the highest Nyquist frequency for which one needs to design the ITER digitizers) signal is 300m, whereas the total wiring length of the sensor+cable system in our test assembly is at the most around 10m. Consequently, a model using conventional circuit elements is feasible.

For the simple 1-pole circuit (model-A in fig6), the AC impedance is easily determined to be:

$Z_A(i\omega) = \dfrac{R_P + sL_P}{1 + (R_P + sL_P)(P_1 + sC_1)} = \dfrac{N_A(i\omega)}{D_A(i\omega)},$	(3)

where $N_A(s)$ and $D_A(s)$ are polynomials in s=iω representing the numerator and denominator of Z_A.

A slightly different physical and numerical approach to determine the equivalent circuit parameters is to consider the measured Z-data as an example of a generalized multi-pole resonant system (i.e. not necessarily representing a driving-point impedance measurement), for which then the transfer function can be given as [15c]:

$$H(i\omega)=\sum_{p=1}^{k}\frac{\alpha_p+i\beta_p\,\omega/\omega_{0,p}}{1+\left(\omega/\omega_{0,p}\right)^2\left(2i\gamma_p/\omega-1\right)}=\frac{A_{(2k+1)}(i\omega)\rightarrow A_{(2k+1)+2j}(i\omega)}{B_{2k}(i\omega)}+D_l(i\omega), \quad (4)$$

where α_p and β_p are fit parameters, and γ_p and $\omega_{0,p}$ are the bandwidth and self resonant frequency, respectively, for each one of the poles p=1→k. Now a numerical fit can be performed, which can be expressed in terms of a rational function as $H(s)=A_m(s)/B_n(s)+D_l(s)$, where D represent a direct (non-resonant) coupling contribution, expressed as a polynomial in s=iω of arbitrary l-order. The order of the denominator $B_n(s)$ is fixed as n=2k, whereas the order of the numerator $A_m(s)$ can be in the range m=(2k+1)→(2k+1)+2j, with j an integer number. This gives more numerical flexibility in modeling the circuit and sometimes helps in overcoming the computational difficulties than one may find when using a (numerically simple) ladder-type instead of the (numerically complex, and never analytically solvable, although more exact in principle) distributed-elements circuit model.

The impedance measurements were obtained in the frequency range 10kHz→13MHz (i.e. just above the minimum and up to the maximum frequencies at which the internal calibration of the instrument used for the measurement is valid). The self-resonant frequency and bandwidth are $\omega_0=1/(L_{SELF}C_{SELF})^{1/2}$ and $\gamma=(\omega_0)^2(R_{SELF}C_{SELF}+P_{SELF}L_{SELF})/2$, respectively: here [$R_{SELF}$, L_{SELF}, C_{SELF}, P_{SELF}] are the frequency-dependent self-resistance, self-inductance, self-capacitance and parallel self-admittance, respectively. However, based on previous analysis of conventional prototypes [4], we have used a frequency-independent value $P_{SELF}=10^{-6}[\Omega^{-1}]$ for the parallel self-admittance, taking it as the inverse of the measured DC isolation resistance value, $P_{SELF}=1/R_{ISOL\text{-}DC}$.

Figure7 shows in a log10-log-10 scale the measured Z-data for some of the prototypes we designed and built (codenamed "*as-built*" in the following), to be compared with the data *calculated* using the design geometry, which will be shown in fig10; the data for a few of the cases for the same

variant are not shown to avoid over-crowding the graphics. First, we note that when more than one prototype was built with the same design, their impedance data are effectively the same, with no more than a 5% difference over the entire frequency range of the measurements. This proves the reproducibility and reliability of our in-house manufacturing of LTCC devices, and gives us greater confidence in being able to obtain precise scaling of the electrical properties of the LTCC sensors, independently of our production processes. Second, the self-resonance frequency clearly decreases from $\omega_0/2\pi$~10MHz for the different variants of the sensors with MM=5 turns on the xy-plane and NN=2 spiral layers, to $\omega_0/2\pi$~(1÷2)MHz for sensors with MM=20 turns and NN=4→10 spiral layers, as the total number of *windings = turns × layers* increases, hence the self-inductance. On the other hand, the scaling of the bandwidth, hence of the quality factor, of the sensor is more complex as it depends on the different effect on the self-inductance of increasing the number of turns in the xy-plane (MM) and of spiral layers along the z-axis (NN) separately. This can be understood easily from fig3, where is it is clear that when adding turns on the same layer (i.e. increasing MM), we do this inside the already existing turns, hence we add progressively less flux-linking area, then giving a progressively smaller contribution to L_{SELF}. On the other hand, when keeping MM constant, and increasing NN (i.e. adding spiral layers), the flux-linking area progressively increases.

The frequency-dependent value of the effective area $(NA)_{EFF}$ for these prototypes has been obtained combining Helmholtz coil and impedance measurements, as described in Appendix-A of [4]; three estimates for the frequency-independent value of $(NA)_{EFF}$ have been separately calculated using two different approaches. First, we have considered a rectangular and elliptical approximation to the exact geometry of the turns in the xy-plane, adjusting numerically the dimensions of these two simpler shapes so as to keep the same total area and winding length in the *model* and in the *as-built* prototypes for each turn on each xy-plane for each spiral layer (note that the contribution of the *vias* is completely neglected when using these two numerical shapes). Figure8 shows an illustrative sketch of these two models for the 1-turn geometry in the xy-plane. The main difference between these approaches comes from the numerical algorithm used to evaluate the inductance of the quarter-circular corner in the design, which affects the value of $(NA)_{EFF}$. In terms of computational

speed, the rectangular model is the fastest one, the elliptical model takes ~7 times more CPU time, and the calculations performed using the exact winding geometry (including as well all the *vias*) take ~83 times more CPU time. Second, we can estimate the effective area by comparing the values of the AC (i.e. derived from the impedance measurements) and DC (i.e. derived using the geometry of the sensor) inductance, since by definition we have that $L(\omega)=d\phi_{TOT}(I,\omega)/dI(\omega)$, where $\phi_{TOT}(I,\omega)$ is the total magnetic flux produced by the current $I(\omega)$ and linked through the effective area of the magnetic sensor. As $\phi_{TOT}(I,\omega)$ can be computed directly using a nominal current element $dI(\omega)$ and the exact geometry of the sensor's solenoidal winding, the solution of the Ampère's law provides another estimate for $(NA)_{EFF}$ through determining the sensor's inductance from the measured impedance. For this evaluation of $(NA)_{EFF}$, we have used for simplicity the value of the inductance as obtained from the measured $Z(\omega)\sim\omega L$ at $\omega=2\pi\times100$kHz, where phase$(Z(\omega))\sim+90$deg.

In summary, we can compare the direct measurement and three different estimates for $(NA)_{EFF}$, and these are shown in fig9(a,b) for all the prototypes for which the impedance data are shown in fig7. First, we note the good agreement between the measurements and the nominal geometrical value of $(NA)_{EFF}$, as shown in fig9a, at least up to ~200kHz: at higher frequencies, there is a clear reduction in $(NA)_{EFF}(\omega)$. There is also a good agreement between the three different estimates of $(NA)_{EFF}$, as shown in fig9b. The data obtained using the simpler rectangular model for the shape of the turns in the xy-plane is always slightly higher than the other two estimates. It is remarkable that both model geometries give very similar results up to MM=20 for $(NA)_{EFF}$, meaning that the effect of the corners, where the *model* differs more from the *as-built* design, is very limited, proving the validity of our very much simplified geometrical approximation to the actual winding shape of the LTCC sensor in the xy-plane.

(IV) Analysis of the electrical characteristics of the LTCC sensors

The measured impedance data for the LTCC prototypes have been analyzed using the circuit model described in Appendix-A, giving the values of $[R_{SELF}, L_{SELF}, C_{SELF}]$. Since in our test equipment the length of the free wire in excess of the winding length is very small (around 10cm, compared to

~8m for the winding length), the best (and simplest) equivalent circuit that can be used to model the real sensor has only one pole, i.e. the one presented at the top of fig6. This can be mathematically represented via rational functions of order 3/2 (direct Z-data fit) or 5/2 (when using the numerical approach leading to eq(4)). Note that these data can also be evaluated analytically for the *equivalent solenoid-like model sensor* with an elliptical or rectangular cross-section for the turns in the xy-plane. With the words "*equivalent solenoid-like*" we mean a *model sensor* which has the same solenoidal shape (i.e. a certain number of turns in the xy-plane replicated on successive spiral layers aligned along the z-axis) and exactly the same total surface area and wiring length of the *as-built sensor* when the shape of the turns in the xy-plane used in the calculations is not the *as-built* one, as sketched in fig8. This approach is useful as it confirms the estimate of these data from the impedance measurements, and provides many empirical insights into the scaling of the electrical properties as a function of the main design choices. Specifically, such "geometrically" obtained data for $[L_{SELF}, C_{SELF}]$ are taken to be the DC (zero-frequency) limit of their AC (frequency-dependent) values, evaluated using the Z-data.

As examples of this good agreement obtained across the range of the LTCC sensors we have built in house, fig10(a-d) show the comparison between the measured Z-data and those calculated, using elliptical and rectangular geometries and the 3/2 and 5/2 rational function fits, for the prototypes with 5turns/4layers/double-thickness (label: 5t4cd), 10turns/4layers (label: 10t4c1), 20turns/8layers (label: 20t8c) and 20turns/4layers-staggered/double-thickness sensors (label: 20ti4cd), respectively. Specifically, we note that the rectangular and elliptical models give results which are very close to the measured Z-data over the entire frequency range of this scan, i.e. from 10kHz to 13MHz. The numerical 3/2 and 5/2 rational function fits also give in general good results but only for frequencies above ~100kHz: this is only partially due to the numerical convergence of this algorithm, which progressively deteriorates when the frequency decreases. This discrepancy starts manifesting itself at higher frequencies for sensors with a smaller total winding length, and it is actually larger for the cases where a ceramic substrate with double-thickness and/or staggered spiral windings were used. This indicates that the usual ladder-type circuit model, which has fully proven its effectiveness and

accuracy for the conventional Mirnov-type prototypes [4], may be of more limited applications for ceramic encapsulated devices, as it cannot correctly approximate distributed electrical parameters such as the sensor's self-inductance and self-capacitance. This is also one of the main factors that have led us towards manufacturing many different prototypes in order to develop and benchmark alternative, geometry-based models for the electrical characteristics of these LTCC sensors.

To estimate the sensor's self-capacitance, we consider the model of a series of electrically insulated planar metallic layers, i.e. the turns in two ceramic substrates at a certain fixed distance making up one *pancake*, and summing up in series all possible combinations of similar pancakes. Then, we add in parallel the sum of all other *pancakes* for which the ceramic substrates are at a different distance, which gives the total capacitance C_{TOT} as a function of the single pancake capacitance $C_{PANCAKE}$ as:

$$C_{TOT} = C_{PANCAKE} \times \sum_{kk=1}^{NN-1} \frac{1}{kk\left(NN-kk\right)},\ C_{PANCAKE} = \varepsilon \frac{1}{SS} \frac{LEN_{TOT} * dd}{NN}. \qquad (5)$$

Here $\varepsilon=\varepsilon_0\varepsilon_r$ is the dielectric permittivity of the green tape (ε_0 and ε_r being the vacuum and relative permittivity, respectively), NN is the number of spiral layers, SS is the thickness of each ceramic substrate, LEN_{TOT} is the total wiring length and dd=200μm is the width of each single track of the wiring in the xy-plane. For this formulation, we have also used the fact that the thickness of the wiring tracks (=10μm) is much smaller than the distance between the tracks along the z-axis SS=(1÷2)×220μm (which in fact corresponds to the thickness of the ceramic substrate), so that we can use the approximation of a thin planar capacitor.

Table3 shows the values of the electrical parameters as extracted from the impedance measurements and as computed using the above-mentioned elliptical and rectangular approximation to the shape of the turns in the xy-plane. In general, there is a good agreement between the various estimates for the main electrical parameters for these prototypes. The discrepancies between the rectangular and the elliptical models and the measurements are actually bigger than what may appear with a cursory look at the data presented in Table3, as shown in more detail in fig11 and fig12. Note specifically that, even if strictly speaking incorrect as all the turns are in fact electrically connected through the

vias, the plane capacitor model used to determine C_{TOT} is in sufficiently good agreement with the value of the capacitance as determined from the measured AC impedance of the sensor when considering all *pancakes*. Conversely, had we used just the closest neighbors, C_{TOT} (now $C_{PANCAKE}$) would have typically been underestimated by a factor 3÷5. Staggering the turns in the odd/even layers only marginally decreases the sensor's self-capacitance and self-inductance as each turn-area is different, typically by no more than 5%, which in turn does not change much ω_0 nor γ.

Looking now in more details at the data shown in fig7, fig9 and Table3 with a view to find the best combination of design options, we find that only two of the sensors (the 20-turns/8-layers and the 20-turns/10-layers) have a sufficient effective area, $(NA)_{EFF}>0.05m^2$. The problem with those two sensors is that their self-resonance frequency is far below the optimum value, since we have $\omega_0/2\pi$=1.2MHz and $\omega_0/2\pi$==1.1MHz, respectively, as their self-inductance is simply too high, $L_{SELF}>400\mu H$ and $L_{SELF}>700\mu H$ for these two cases. Conversely, if we consider the sensors with a sufficiently high self-resonance frequency, such as the 5-turns/4-layers, for which $L_{SELF}\sim30\mu H$ and $\omega_0/2\pi$=(7÷8)MHz, the corresponding effective area is too small, $(NA)_{EFF}\approx0.01m^2$. It is therefore clear that the total number of turns MM×NN and their geometrical arrangement must be optimized to preferentially increase the effective area instead of the sensor's self-inductance, as obviously both L_{SELF} and $(NA)_{EFF}$ increase for increasing values of MM×NN.

Starting from the good agreement obtained between the Z-data measurements and the calculations using the rectangular and elliptical models, and noting that our in-house production processes for these prototypes is now only developed around a fixed, almost square, shape for the DuPont951 green tape (of size ~60mm) that is then cut in four similar sections (of sizes ~(30×30)mm), it is clear that the three most important design optimization parameters are the separation between the spiral layers, the number of turns in each layer and the total number of layers. Hence, a numerical scan of the individual effect of each of these parameters separately on the electrical characteristics of the LTCC sensors has been performed, using the value of the self-capacitance as obtained by summing over all possible combinations of *pancakes*, as shown in fig11(a-c).

The first important point to note is the good agreement between the calculations performed using the elliptical model and the exact solenoidal shape for the turns in the xy-plane. Conversely, it is clear that the rectangular model is less accurate: this is because the very fast numerical algorithm used to compute the self-inductance for this geometry largely over-estimates the contribution of the flux-elements close to the corners, with the effect becoming more important for increasing values of MM. This does not happen when using the elliptical model, as the resulting elliptical functions used to evaluate L_{SELF} can be solved numerically with a high degree of accuracy. Although much faster computationally, the rectangular model for the shape of the turns in xy-plane can only give a coarse estimate for the electrical properties of the LTCC sensors.

Examining now in detail the results presented in fig11a, we note that, essentially as expected, increasing the inter-layer separation, for instance by adding a neutral layer between the conductive layers, does not change the effective area of the sensor, but brings about a very beneficial linear increase in the self-resonant frequency by reducing the self-inductance (~linearly) and the self-capacitance (~exponentially). When increasing the number of spiral layers (NN) along the z-axis, as shown in fig11b, we find that the effective area and the self-inductance both increases (almost linearly and almost quadratically, respectively), whereas the self-capacitance decreases. When increasing the number of turns (MM) in the xy-plane, as shown in fig11c, we find that C_{SELF}, L_{SELF} and $(NA)_{EFF}$ all increase, but appear to saturate at higher values of MM. Finally, when comparing in greater details the results of fig11b with those of fig11c, it is clear that increasing $(NA)_{EFF}$ without increasing too much the self-inductance, hence reducing excessively its self-resonant frequency, is best accomplished by increasing the number of spiral layers (NN) along the sensor z-axis than the number of turns (MM) in the xy-plane.

(V) Scaling laws for predicting the electrical characteristics of the LTCC sensors

Following the analysis of the impedance measurements, we can now derive empirical scaling laws for the electrical characteristics of the LTCC sensors as function of the main design parameters we can vary in our in-house production processes. Figure12(a-c) show the best scaling fit to the

calculated sensor's effective area, self-resonance frequency, self-inductance and self-capacitance as function of the number of turns in the xy-plane (MM), the number of spiral layers (NN) and the inter-layer separation (SS). Note that SS is not necessarily the thickness of the ceramic substrate, as we consider the option of adding a number of neutral layers between those screen-printed with the conductive ink. For these calculations, we have used the fixed geometry described above for the ceramic substrate and for the track width, thickness and separation, as in fig9 and fig10.

First, from fig12a we note that the results from the rectangular model for the xy-planar winding become progressively more in disagreement with those obtained with the elliptical model and the exact shape of the turns as MM increases. Hence, it is clear that for optimizing with a numerically efficient algorithm the design choices to obtain an LTCC sensor of sufficient effective area, the best option is to use the elliptical approximation to the shape of the turns in one single layer in the xy-plane, as this algorithm is >12 times faster than the one using the exact solenoid winding shape.

Second, going into the details of the best scaling formula, we obtain that:

1. fig12a ➔ electrical data as function of the number of turns on the xy-plane MM for fixed SS=220μm and NN=5: $(NA)_{EFF} \sim L_{SELF} \sim C_{SELF} \propto const \times (1-\exp(-MM/12))$, $\omega_0 \propto (1-\exp(-MM/12))^{-1}$, which then further simplifies to $\omega_0 \propto 12/MM$ for the foreseen range MM=[3÷7];
2. fig12b ➔ electrical data as function of the number of spiral layers along the z-axis NN for fixed SS=220μm and MM=10: $(NA)_{EFF} \propto NN^{0.9}$, $L_{SELF} \propto NN^{7/4}$, $C_{SELF} \propto NN^{-5/9}$, hence $\omega_0 \propto NN^{-4/7}$;
3. fig12c ➔ electrical data as function of the inter-layer separation along the z-axis SS for fixed NN=5 and MM=10: $(NA)_{EFF} \propto SS^{0}$, $L_{SELF} \propto SS^{-1/3}$, $C_{SELF} \propto 1/SS$, hence $\omega_0 \propto SS^{2/3}$.

The precise scaling law $L_{SELF} \propto SS^{-1/3}$ is not at all trivial but can be simply understood in terms of the change in magnetic flux linked by the turns in the xy-plane as the separation between the different spiral layers along the z-axis is increased. Similarly, the scaling law $C_{SELF} \propto NN^{-5/9}$ depends on the ratio between the number of parallel and series *pancakes*, and it would have been difficult to predict it precisely *ab-initio*, although this value is sufficiently close to the relation $C_{SELF} \propto NN^{-1/2}$ that would have been suggested by a simple combinatorial analysis, only for a much higher value of

NN>50. The very similar relation (but for a different constant multiplication factor) that we have found in the scaling laws for [L_{SELF}, C_{SELF}, $(NA)_{EFF}$] as $\propto$const$\times$(1-exp(-MM/12)) is also non trivial as we have increased the number of turns on the xy-plane while keeping the same overall planar dimensions of the green tape, i.e. by adding further turns *inside* the already existing ones. While it is obvious that a point will be reached where the relative increase in the total enclosed area becomes too small to produce any noticeable effect, its precise determination (in our case: MM=12) is very difficult to obtain *ab-initio* as it will depend on the exact geometrical details of the green-tape, of the track width and of their separation. The scaling laws $L_{SELF} \propto NN^{7/4}$ and $(NA)_{EFF} \propto NN^{0.9}$ follow very closely the expected dependencies for a solenoid-like magnetic sensor: $(NA)_{EFF} \propto NN$ and $L_{SELF} \propto NN^2$, the differences being related to the fact that the xy-planes are not fully packed along the z-axis, but are separated by the thickness of the ceramic substrate, allowing some magnetic flux to escape. Finally, it is important to note that the effect of the mutual coupling between the different tracks and *vias* appear to be small for these single-axis sensors, as the scaling of their electrical properties in many aspects follows sufficiently closely that which would have been expected from the standard electro-magnetic circuit theory applied to a solenoid-like winding.

(VI) Summary and conclusions

This paper presents the results of the prototyping of an HF inductive magnetic sensor built using the LTCC technology, and aimed at satisfying the ITER measurement requirements for HF magnetic instabilities. Our work has focused on three main activities, i.e. (1) designing and manufacturing in-house different LTCC sensors around a baseline design, (2) measuring their electrical properties, and (3) determining and benchmarking scaling laws for such electrical properties as function of the main design parameters that would allow us to confidently predict the electrical properties of future inductive magnetic sensors manufactured using the LTTC technology.

The LTCC HF magnetic sensors have been prototyped in-house very quickly (taking about 1 month between the initial design and the end of the electrical testing program) and at very reasonable cost, around ~200USD each (which includes the raw material, the different screen prints for each sensor

design, the pro-rata running costs for the use of the furnace where the LTCC are fired, and some radiography for the sensors that were found to be open circuit after the firing, but not our pro-rata salary costs). This has allowed us to assess very efficiently many different design options, the only drawback being the somewhat limited choice of available materials for the green-tape (DuPont951) metallic ink (silver), and track and *vias* geometry.

Using the measurement of the sensor impedance, we have been able to develop and benchmark an adequate circuit model for these sensors, which has led us to obtain empirical scaling laws for the main electrical characteristics (self-inductance, self-capacitance, effective area) as function of the design parameters that we could change easily with our in-house manufacturing, i.e. the number (NN) and separation (SS) between adjacent spiral layers along the sensor (longitudinal) z-axis, and the number (MM) of turns in the (perpendicular) xy-plane. For fixed NN and SS values, we find the non-trivial scaling laws $(NA)_{EFF} \sim L_{SELF} \sim C_{SELF} \propto const \times (1-\exp(-MM/12))$, which are related to the progressively smaller increase in the enclosed area as further turns are added on the xy-plane. For fixed MM and SS values, we find the scaling laws $(NA)_{EFF} \propto NN^{0.9}$, $L_{SELF} \propto NN^{7/4}$ and $C_{SELF} \propto NN^{-5/9}$, which are very close to those expected for a multi-turns solenoid-like magnetic sensor. Finally, for fixed NN and MM values, we find that $(NA)_{EFF} \propto SS^{0}$, $C_{SELF} \propto 1/SS$ and $L_{SELF} \propto SS^{-1/3}$: whereas the first two laws are as those expected from a simple electrical circuit model, the scaling of L_{SELF} vs. SS is non-trivial as it depends on the ratio between the magnetic flux which is linked by the turns on the xy-plane and that which escapes as such turns are not fully packed along the z-axis. Using these fully validated empirical scaling laws, we are now able to proceed with greater confidence towards developing an LTCC sensor which meets the ITER measurements requirements. Note also that, although specifically developed for LTCC-based HF magnetic sensors for ITER, our circuit model approach is of a more general validity, and in principle can be applied to other LTCC magnetic sensors as well as to similar devices built upon the HTCC technology.

Considering now specifically the ITER measurement requirements, our prototyping and electrical testing program has clearly shown that an optimum compromise can be achieved between different design choices so that an LTCC HF inductive magnetic sensor can be manufactured with a

sufficiently high effective area $(NA)_{EFF}>0.05m^2$, a moderate self-inductance $L_{SELF}<100\mu H$ and a sufficiently small self-capacitance $C_{SELF}<60pF$ to give a high self-resonant frequency $\omega_0/2\pi>5MHz$. Using a fixed size for the *green tape*, these objectives can be achieved by the following two steps:

(1) increase interlayer separation SS, for instance by adding a neutral layer between the conductive layers ➔ this reduces linearly L_{SELF} and reduces exponentially C_{SELF} for a fixed $(NA)_{EFF}$;

(2) increase the number of spiral layers NN for a fixed number of turns MM=5÷7 ➔ this increases linearly $(NA)_{EFF}$ while increasing L_{SELF} just less than quadratically.

Hence, these two steps can be used to guide the design towards future 1D LTCC prototypes with the aim of reducing the increase in the sensor self-inductance LSELF while maximizing the effective area $(NA)_{EFF}$, which are both beneficial to the measurement performance of such sensors.

Taking now into account the volume occupation constraints for the HF magnetic sensors in ITER, it is currently foreseen to install these sensors within ad-hoc cutouts in the blanket modules, with size ~(50×50×50)mm, and/or in the almost continuous but very thin gap (of thickness <10mm) between the blanket and the first vessel wall. As an example of a device meeting the ITER measurement requirements, an LTCC sensor with inter-layer separation of ~600μm (using two neutral layers between each conducting substrate), MM=5 turns and NN=12 spiral layers built with silver ink using a standard Dupont951 green tape with a ~(30×30)mm planar size (i.e. occupying about 5% of the volume of the conventional Mirnov-type sensor currently foreseen for ITER), is predicted to have $(NA)_{EFF}\approx0.05m^2$, $L_{SELF}\approx90\mu H$, $C_{SELF}\approx10pF$ and $\omega_0/2\pi\approx6MHz$. Considering now a 50m-long signal cabling with the foreseen lower limit for the cable's self-capacitance C_{CABLE}~10pF/m and a rather typical value for the self-inductance L_{CABLE}~0.3μH/m [11, 16], this sensor+cabling system would have a predicted self-resonance frequency $\omega_0/2\pi\approx700kHz$ at the front-end electronics. Therefore, not only the electrical properties of this sensor would satisfy the ITER measurement requirements, but this device would have a thickness of ~8mm and a ~(30×30)mm planar size, which can fit in all the currently foreseen locations in ITER for such HF magnetic sensors. LTCC sensors with such optimized geometrical parameters are currently being detailed designed for in-

house prototyping in the near future.

(VII) An outlook towards future activities

Looking now towards future activities, it is clear that further prototyping studies are required before a design can be finalized for the HF magnetic sensors proposed for use in ITER. Comparing the ceramic encapsulated technology presented here with the Mirnov-type design analyzed in [4, 5], one of the main advantages of the HTCC and/or LTCC sensor resides in its much smaller size, as this allows for a significant reduction in the space occupied by the measurement device and removes all difficulties related to the manufacturing of a complex ceramic body and the assembly of a winding pack onto it that are associated with an HF magnetic sensor of conventional Mirnov-type design. Moreover, as an alloy is formed between the ceramic and the metallic ink, the sensor becomes very compact and vacuum tight, further reducing the risk of out-gassing and breakages of its inner components. As described in Section-II, when comparing the relative advantages and drawbacks of the HTCC and LTCC technologies, and the operational experience obtained with such sensors in different devices, it is our clear view that LTCC devices are a more practical choice than HTCC ones for installation on ITER, hence the focus of our future activities is solely on LTCC sensors.

Increasing the LTCC device thickness from ~2.4mm (current prototypes, which can only separately meet the ITER measurement requirements on effective area and frequency response) to ~8mm (as shown above: predicted to meet jointly all the ITER measurement requirements) will also make it *relatively straightforward* to design and prepare the screen-prints for a 3D winding to measure the complete set of three-axial components of HF magnetic fluctuations. An example of a preliminary design for such a 3D sensor is given in fig13. For this design we are considering the use of a full size Dupont951 ceramic substrate, with unfired dimensions of ~(60×60)mm, which maximizes $(NA)_{EFF}$ for the x- and y- measuring axis. The main limitation of this design is the very large number of interlaced conducting tracks and *vias* (about 8'500), which not only makes the print-screens for the various layers all different to each other, but also increases the risk of loosing

electrical continuity throughout the sensor. This design is now being further optimized, specifically by adding a number of "connection" points to test, after the firing process, the electrical continuity between smaller subsections of the winding, and possibly "bridge across" any such faulty section of the tracks and *vias*, so that an electrical fault during the production of the sensor would only result in a (hopefully) minor change in the sensor's electrical properties and not in the loss of the entire sensor. We are also looking at simplifying the design of the different layers, so that a smaller number of screen-prints would be required. This would make in principle such designs much easier to be scaled-up for industrial-scale and fully quality-controlled production through out-sourcing. Some further improvements are also required for our in-house production processes, particularly with respect to the control of dust and building-up of static electricity on the unfired layers in our university-standards clean room, which was found to be the cause of the small number of electrical faults in the 1D sensors we have already prototyped. Another more conceptual difficulty arises due to mutual coupling between the now much larger number of tracks and *vias*, which can affect the sensor's electrical properties in ways that we could not have found with our existing single-axis sensors. This may prompt for a 3D adaptation of our electrical models.

As briefly discussed in Section-II, the main difficulty with the LTCC technology is related to the metallic ink used to print the circuit onto the green tapes, as current manufacturing processes mainly use silver and gold, whereas such materials may have to be avoided for use for ITER in-vessel components due to a perceived risk of neutron-induced transmutation to cadmium and mercury. Further in-house R&D and prototyping activities are now planned to assess the use of different metallic inks, such as platinum and palladium, and ceramic materials. Possible materials foreseen for the ceramic substrates are the ESL 41110-70C, with lower relative dielectric constant ε_r=4.3÷4.7 (compared to ε_r=7.8 for the DuPont DP-951), which would correspondingly increase the resonant frequency for the same (NN, MM, SS) winding arrangement by approximately 30%, or the DuPont DP-943, which has a lower coefficient of thermal expansion CTE=4.5ppm/K (compared to CTE=5.8ppm/K for the DuPont DP-951), which would reduce the thermal loading on the assembly.

A dedicated materials and radiation testing program is also currently foreseen ex-house to confirm the suitability of the selected materials for use in ITER.

Acknowledgements

This work was partly supported by the European Communities under Contracts of Association, and was partly performed within the framework of the European Fusion Development Agreement, under Task TW6-TPDS-DIADEV. The views expressed in this publication are the sole responsibility of the authors and do not necessarily reflect the views of Fusion for Energy or the European Commission. We would like to acknowledge the discussions we have had during this work with current members of the ITER organization (A.Encheva, G.Vayakis, C.Walker) and of EFDA and F4E (S.Arshad, C.Ingesson). The authors would also like to thank the Reviewers for their comments and suggestion, which have helped in improving the clarity of our presentation.

References

1. For a general overview of the ITER measurement requirements for the HF magnetic diagnostic system, see: G.VAYAKIS et al., Rev. Sci. Inst. **74** (2003), 2411, and A.J.H.DONNÉ et al., "Chapter 7: Diagnostics", Special Issue of Nucl. Fusion **47** (2007) S337, and references therein; for a general overview on magnetic diagnostic systems see also E.J.STRAIT, E.D.FREDRICKSON, J.-M.MORET, M.TAKECHI, Fus. Sci. Tech. **53**(2) (2008), 304 and references therein and http://crpp.epfl.ch/itermag/index.php/SCI:Bibliography (access: duccio.testa@epfl.ch); see also: Table-2 in the Design Description Document DDD 5.5.A, ITER document reference "N55DDD101-06-12W0.3" (document available by request to: duccio.testa@epfl.ch).
2. For a general overview of the ITER environmental condition and of its operating regimes, see "Progress in the ITER Physics Basis", Special Issue of Nucl. Fusion **47** (2007).
3. D.TESTA et al., *Functional performance analysis and optimization for the high-frequency magnetic diagnostic system in ITER – Part 1: Overview of the Results* and *Part 2: Detailed Overview of the Analysis Method and of the Test Calculations*, Fus. Sci. Tech. **57**(3) (2010), 208-237 (Part-1) and 238-273 (Part-2).
4. D.TESTA et al., *Prototyping the ITER high frequency magnetic sensor using the conventional, Mirnov-type, pick-up coil*, submitted for publication in Fusion Science and Technology.
5. D.TESTA et al., *Baseline system design and prototyping for the ITER high-frequency magnetic diagnostic set*, Proceedings of the 23rd Symposium on Fusion Engineering, 01-05 June 2009, San Diego (USA).
6. H.TAKAHASHI, S.SAKAKIBARA, Y.KUBOTA, AND H.YAMADA, Rev. Sci. Inst. **72** (2001), 3249.
7. E.FREDRICKSON and S.GERHARDT, PPPL (USA), private communication.
8. T.EDLINGTON, CCFE (UK), private communication.
9. G.CHITARIN, R.DELOGU, A.GALLO, S.PERUZZO, Fus. Eng. Des. **84** (2009), 593.
10. ITER Project, Risk Management Plan: documents ITER_D_22F4LE (v1.1), 2EW3E7 (v1.2)

(documents available by request to: duccio.testa@epfl.ch).

11. N.BALUC and C.HOLLENSTEIN, EPFL (CH), private communication.
12. Technical information provided courtesy of G.VAYAKIS, A.ENCHEVA and C.WALKER.
13. For details on the COMSOL software package: http://www.comsol.com/products/.
14. For details on the FEMM software package: http://femm.foster-miller.net/wiki/HomePage.
15. (a) J-M.MORET et al., Rev. Sci. Inst. **69** (1998), 2333 [also see Ref.3 cited therein: J.-M.Moret, "Fitting of transfer functions to frequency response measurements" CRPP Laboratory Report LRP 498/94, Lausanne, 1994]; (b) R.HEETER, A.FASOLI, S.ALI-ARSHAD, J-M.MORET, Rev. Sci. Inst. **71** (2000), 4092; (c) A.FASOLI et al., Phys. Rev. Lett. **75**(4) (1995), 645.
16. A.PEREZ, EPFL (CH), private communication.

Figure Captions

Figure1. The main steps for the manufacturing and screen printing of the LTCC ceramic substrates.

Figure2. Sketch illustrating the difference between normal and staggered winding layers for the conductive tracks in the LTCC sensor design.

Figure3(a-d). Manufacturing drawings for each individual layer of the prototype LTCC sensors, using the nominal 1-turn geometry (fig3a, top left), and the actual 5-turn (fig3b, top right), 10-turn (fig3c, bottom left) and 20-turn geometries (fig3d, bottom right).

Figure4. A 3D view of the 5-turns/4-layers/double-width sensor, to illustrate in more details the assembly of the prototype with the conducting and the *neutral* layers, the inter-layer connections through the filling of the *via* holes, and the connection pad for the ex-sensor wiring, cut in the front right corner at the bottom of the assembly.

Figure5. Some of the LTCC prototype HF magnetic sensors we designed and built in-house.

Figure6. Schematics of magnetic probe circuit models. The "input" (driving voltage from $\partial B/\partial t$) is on the left, and the "output" (which goes to the front-end electronics) is on the right. The "P" terms are for the admittances (parallel resistances, $P_k=1/R_{||k}$) of the transmission cable. Note that a more general formulation for these P-terms for the 2-pole onwards model also includes a frequency dependency due to the parallel inductance of the transmission cables, $P_k(s)=1/(R_{||k}+sL_{||k})$, and it is this formulation which is used in this work. Top: simple single-pole model (model-A) which includes the probe and one set of elements for the effects of the cable, which best corresponds to the prototypes analyzed in this work. Middle: second-order model (model-B) which has 2 sets of parameters for the cable. Bottom: generalization of the circuit model to a k-pole system with an arbitrary number of circuit parameters (model-K).

Figure7. The measured Z-data for some of the LTCC sensors: each prototype is code-named with its number of turns on a plane, the number of layers and then its variant, so that, for instance, the code-name "20ti4c3" indicates the sensor with 20turns, 4 layers staggered (windings in the odd/even layers not superimposed but shifted, i.e. using staggered layers as shown in fig2 on the

right), 3rd prototype; the letter "d" indicates that a layer with double thickness has been used. We have used a log10-log10 scale to better separate graphically the different cases.

Figure8. Exact winding shape and its rectangular and elliptical approximation used to calculate the effective area of the LTCC prototypes, shown here for simplicity for just one turn in the xy-plane; by numerically adjusting the dimensions of the rectangular and elliptical winding, the total area and winding length are kept the same in these two geometrical approximations for an equivalent *model sensor* as in the *as-built* sensors.

Figure9a. The value of $(NA)_{EFF}(\omega)$ for all the LTCC prototypes for which the impedance data are shown in fig7, obtained combining Helmholtz coil and impedance measurements, as described in Appendix-A of [4]; the legend also indicates the nominal geometrical value of $(NA)_{EFF}$, which allows to note the good agreement between the measurements and the expected value for all sensors.

Figure9b. Calculated effective area using the rectangular and elliptical approximation for the winding shape in the xy-plane (as defined in fig8), and as obtained from the impedance measurements at 100kHz, for all the prototypes for which the impedance data are shown in fig7.

Figure10(a-d). Comparison between the measured and calculated Z-data for some of the *as-built* prototypes for the LTCC HF magnetic sensors for ITER: 5turns/4layers/double-thickness (fig10a, top left, label: 5t4cd as in fig7), 10turns/4layers (fig10b, top right, label: 10t4c1), 20turns/8layers (fig10c, bottom left, label: 20t8c) and 20turns/4layers-staggered/double-thickness (fig10d, bottom right, label: 20ti4cd), respectively. For all these prototypes we have used a DuPont951 ceramic substrate, with unfired thickness =220μm, relative dielectric constant and magnetic permeability ε_r=7.8 and μ_r=1, respectively; the metallic ink is silver, and the wire dimensions are =200×10μm (width in the xy-plane times thickness); the separation between two adjacent tracks on the xy-plane is =400μm. For clarity, all these graphs are plotted using a log10 scale for the frequency and magnitude of the Z-data, and a linear scale for the phase of the Z-data.

Figure11a. Scan of the main electrical parameter for an LTCC sensor as function of the inter-layer separation for a fixed number of turns (MM) in the xy-plane and number of layers (NN) along the z-

axis; for this analysis we considered the rectangular, elliptical solenoid models and the exact geometry of the *as-built* design.

Figure11b. Scan of the main electrical parameter for an LTCC sensor as function of the number of layers (NN) along the z-axis for fixed number of turns (MM) in the xy-plane and inter-layer separation; for this analysis we considered the rectangular, elliptical solenoid models and the exact geometry of the *as-built* design.

Figure11c. Scan of the main electrical parameter for an LTCC sensor as function of the number of turns (MM) in the xy-plane for a fixed number of layers (NN) along the z-axis and inter-layer separation; for this analysis we considered the rectangular, elliptical solenoid models and the exact geometry of the *as-built* design.

Figure12a. Calculated empirical scaling laws for the main electrical characteristics of the LTCC sensors, as function of the number of turns on the xy-plane (MM).

Figure12b. Calculated empirical scaling laws for the main electrical characteristics of the LTCC sensors, as function of the number of spiral layers along the z-axis (NN).

Figure12c. Calculated empirical scaling laws for the main electrical characteristics of the LTCC sensors, as function of the inter-layer separation (SS).

Figure13. A CAD drawing of a 3D HF magnetic sensors built upon the LTCC technology, using 10 full size DuPont951 ceramic substrates (i.e. ~600×600μm); the x- and y- measuring windings are staggered so as to separate them as much as possible (reduce stray capacitance and mutual inductance) but do still occupy ~2/3 of the device's thickness so as to have a sufficiently high effective area $(NA)_{EFF}>0.04m^2$; the z-axis measuring windings are concentrated in the central section of the device, again to decouple as much as possible the three measurement axis; note the very large number of interlaced conducting tracks and *vias*, which makes further optimization of this design essential so as to simplify the production process.

Table Captions

Table1. Some of the main electrical and thermal properties of the metallic inks that can be used for magnetic sensors based on the HTCC and LTCC technologies. The temperature coefficient α increases/decreases the significant portion of the resistivity, as $\Delta\rho=\alpha\Delta T\rho_0$ where ρ_0 is the resistivity at 300K, hence $\rho(T)=\rho_0\times(1+\alpha\Delta T)$. The relative magnetic permeability μ_r of the material is defined using the volume magnetic susceptibility χ_M as $\mu_r=1+\chi_M$. Note that χ_M is a signed quantity, such that $\chi_M<0$ and $\chi_M>0$ for diamagnetic and paramagnetic materials, respectively.

Table2. Physical and electrical properties of the material used for the production of the prototype LTCC HF magnetic sensors for ITER.

Table3. Measured and calculated [R, L, C] data for the different LTCC prototypes; the same code-naming as in fig7 is used in this table; the entry "measured $(NA)_{EFF}$ [m^2] from ωL @100kHz" is obtained from solving the Ampère's law for the sensor, as described in Section-III.

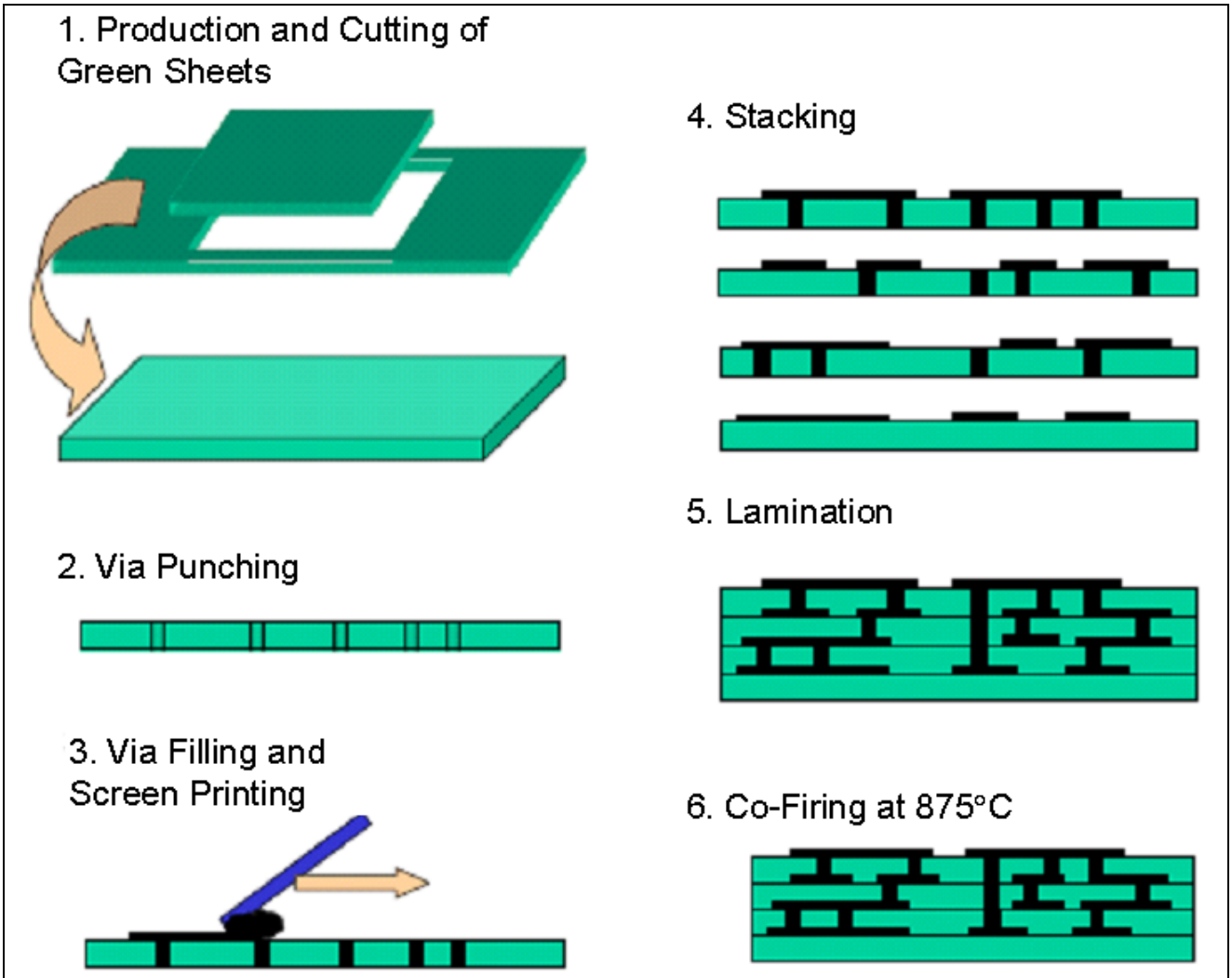

Figure1. The main steps for the manufacturing and screen printing of the LTCC ceramic substrates.

D.Testa, Figure1, MS-356709-V4

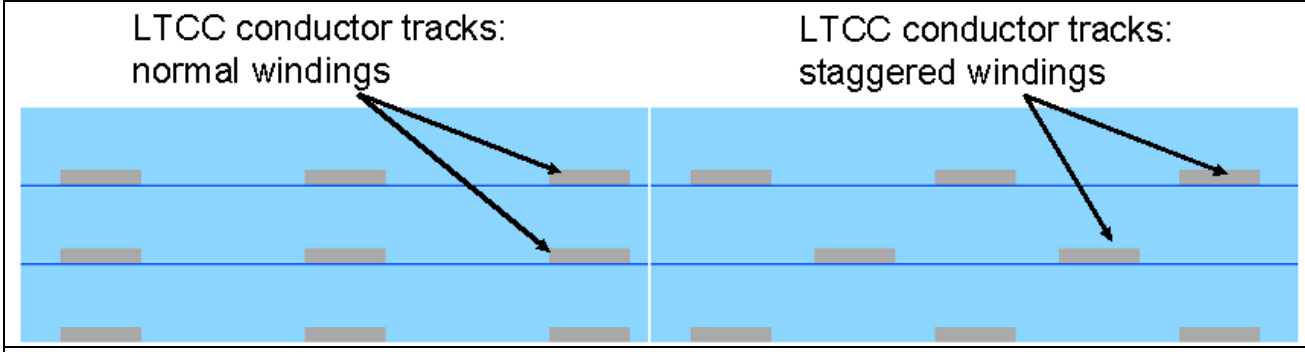

Figure2. Sketch illustrating the difference between normal and staggered winding layers for the conductive tracks in the LTCC sensor design.

D.Testa, Figure2, MS-356709-V4

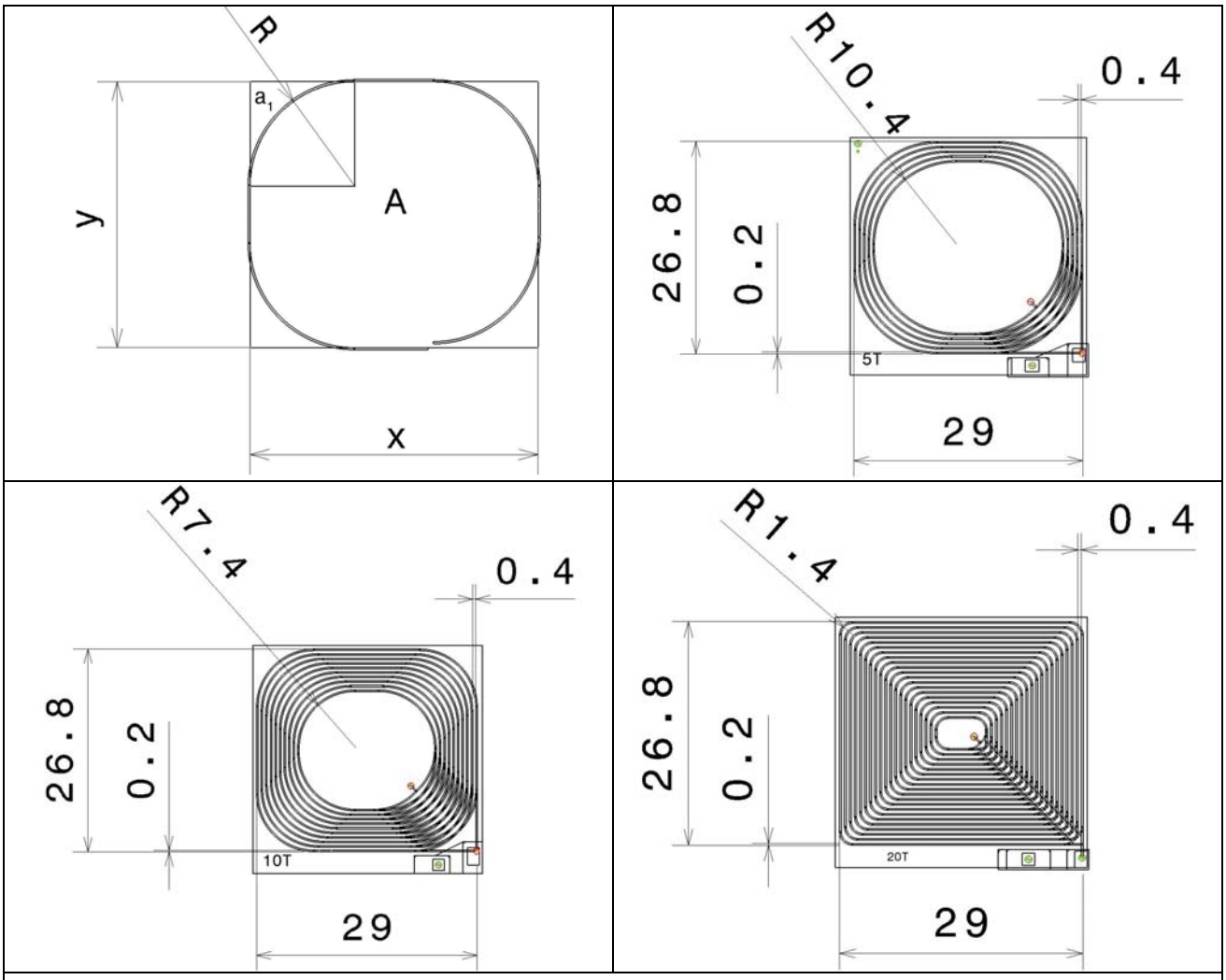

Figure3(a-d). Manufacturing drawings for each individual layer of the prototype LTCC sensors, using the nominal 1-turn geometry (fig3a, top left), and the actual 5-turn (fig3b, top right), 10-turn (fig3c, bottom left) and 20-turn geometries (fig3d, bottom right).

D.Testa, Figure3(a-d), MS-356709-V4

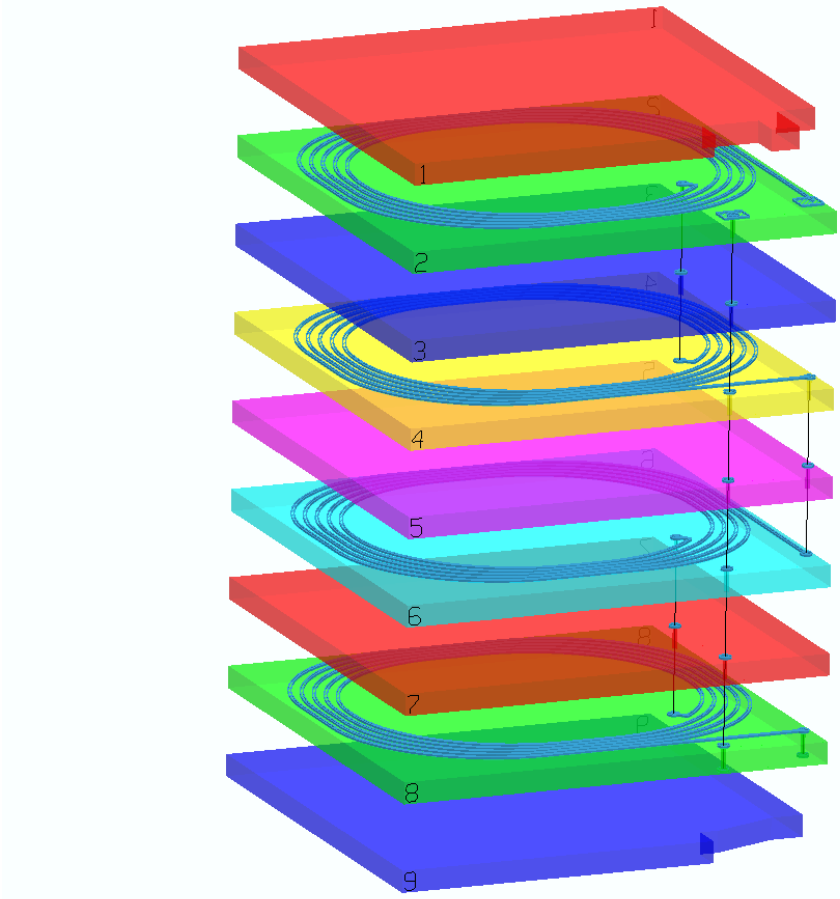

Figure4. A 3D view of the 5-turns/4-layers/double-width sensor, to illustrate in more details the assembly of the prototype with the conducting and the *neutral* layers, the inter-layer connections through the filling of the *via* holes, and the connection pad for the ex-sensor wiring, cut in the front right corner at the bottom of the assembly.

D.Testa, Figure4, MS-356709-V4

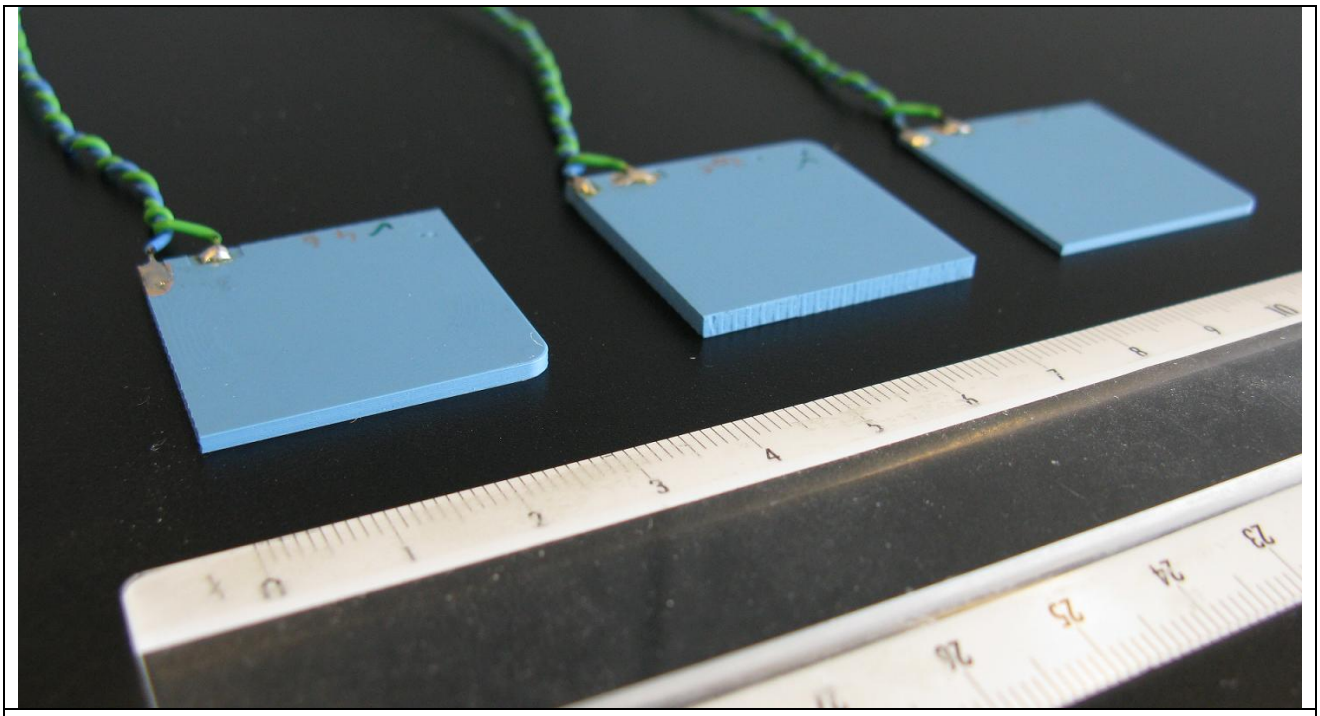

Figure5. Some of the LTCC prototype HF magnetic sensors we designed and built in-house.

D.Testa, Figure5, MS-356709-V4

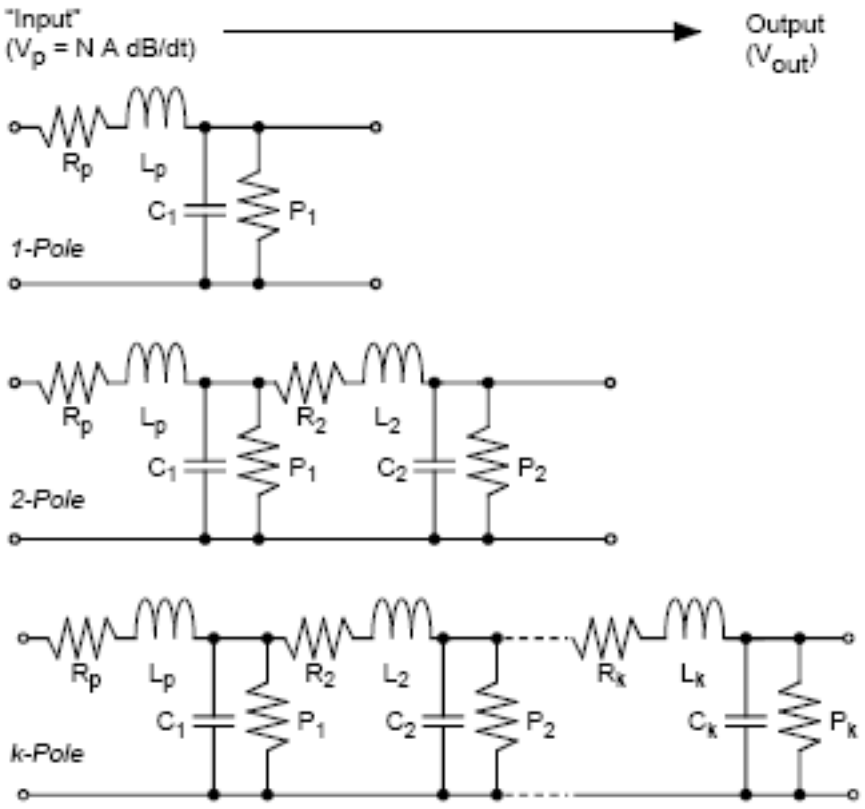

Figure6. Schematics of magnetic probe circuit models. The "input" (driving voltage from $\partial B/\partial t$) is on the left, and the "output" (which goes to the front-end electronics) is on the right. The "P" terms are for the admittances (parallel resistances, $P_k=1/R_{||k}$) of the transmission cable. Note that a more general formulation for these P-terms for the 2-pole onwards model also includes a frequency dependency due to the parallel inductance of the transmission cables, $P_k(s)=1/(R_{||k}+sL_{||k})$, and it is this formulation which is used in this work. Top: simple single-pole model (model-A) which includes the probe and one set of elements for the effects of the cable, which best corresponds to the prototypes analyzed in this work. Middle: second-order model (model-B) which has 2 sets of parameters for the cable. Bottom: generalization of the circuit model to a k-pole system with an arbitrary number of circuit parameters (model-K).

D.Testa, Figure6, MS-356709-V4

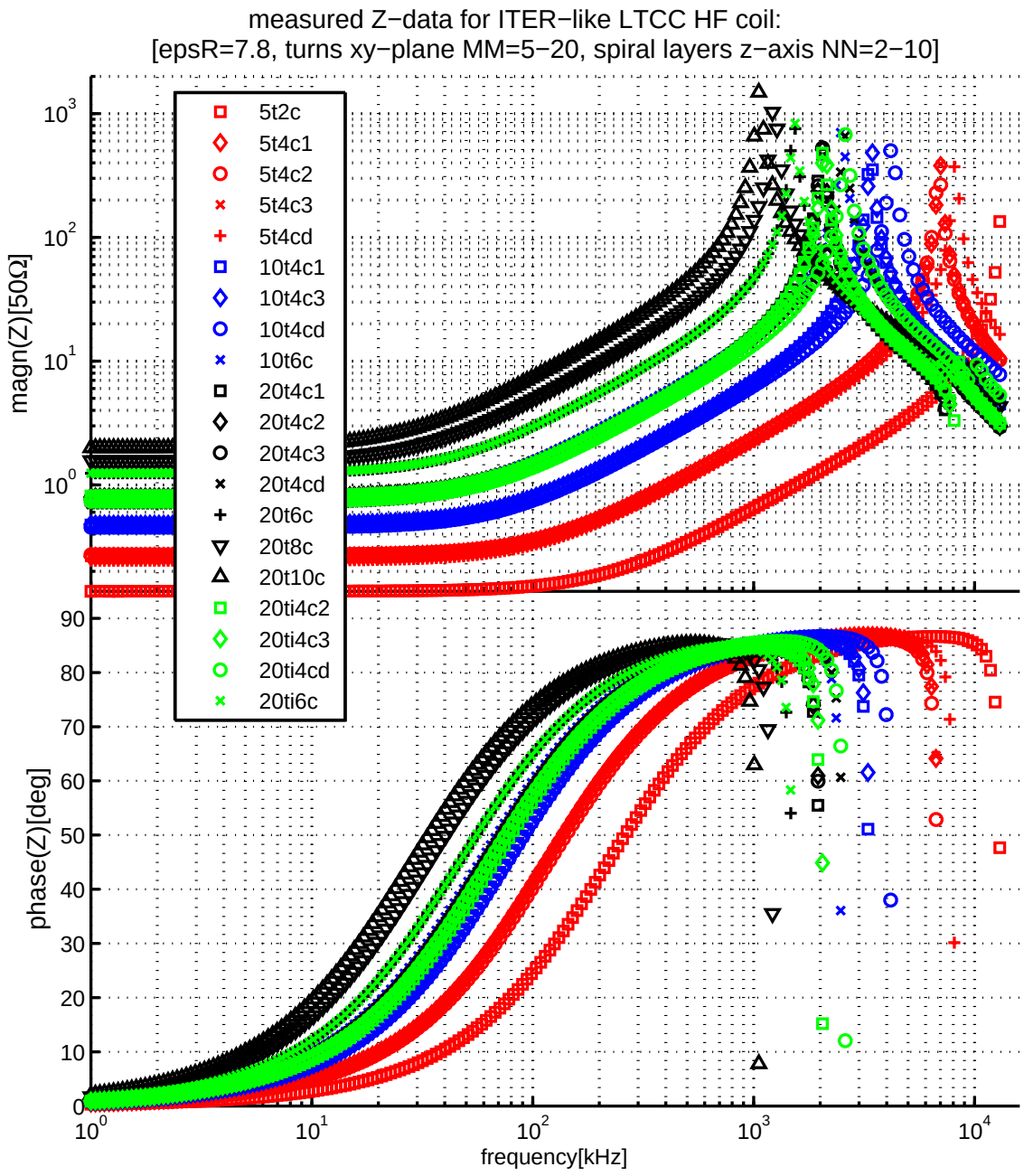

Figure7. The measured Z-data for some of the LTCC sensors: each prototype is code-named with its number of turns on a plane, the number of layers and then its variant, so that, for instance, the code-name "20ti4c3" indicates the sensor with 20turns, 4 layers staggered (windings in the odd/even layers not superimposed but shifted, i.e. using staggered layers as shown in fig2 on the right), 3rd prototype; the letter "d" indicates that a layer with double thickness has been used. We have used a log10-log10 scale to better separate graphically the different cases.

D.Testa, Figure7, MS-356709-V4

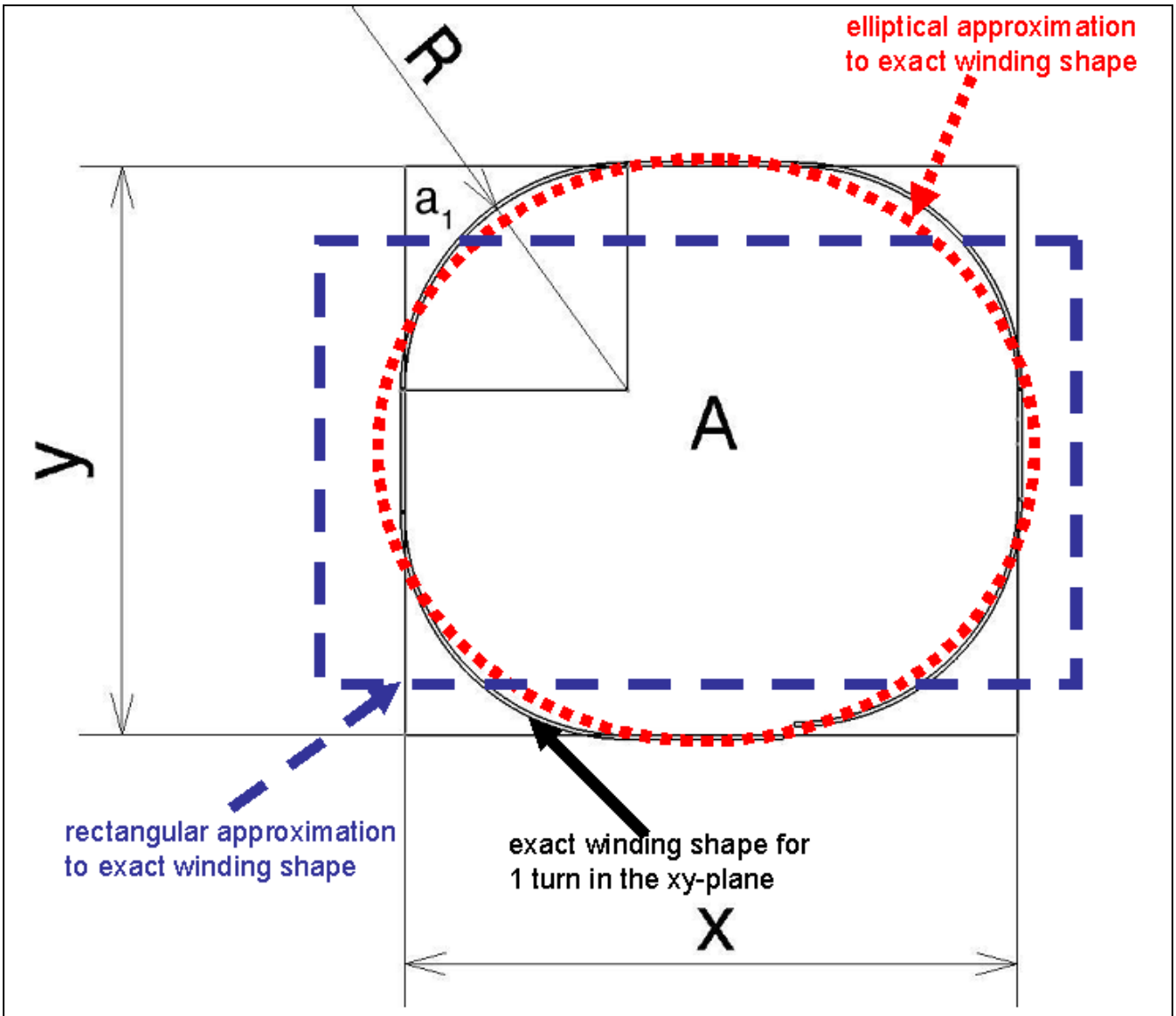

Figure8. Exact winding shape and its rectangular and elliptical approximation used to calculate the effective area of the LTCC prototypes, shown here for simplicity for just one turn in the xy-plane; by numerically adjusting the dimensions of the rectangular and elliptical winding, the total area and winding length are kept the same in these two geometrical approximations for an equivalent *model sensor* as in the *as-built* sensors.

D.Testa, Figure8, MS-356709-V4

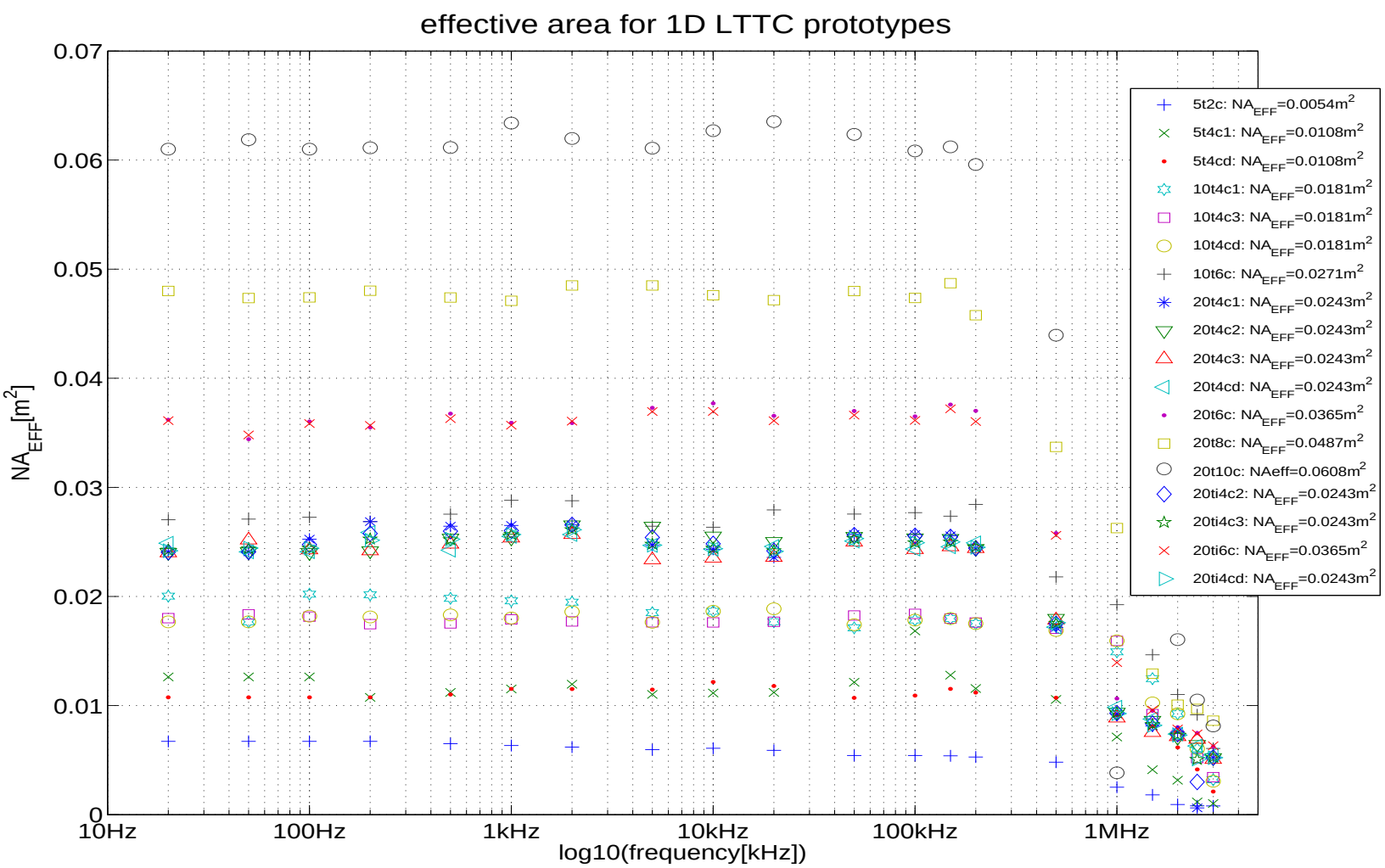

Figure9a. The value of $(NA)_{EFF}(\omega)$ for all the LTCC prototypes for which the impedance data are shown in fig7, obtained combining Helmholtz coil and impedance measurements, as described in Appendix-A of [4]; the legend also indicates the nominal geometrical value of $(NA)_{EFF}$, which allows to note the good agreement between the measurements and the expected value for all sensors.

D.Testa, Figure9a, MS-356709-V4

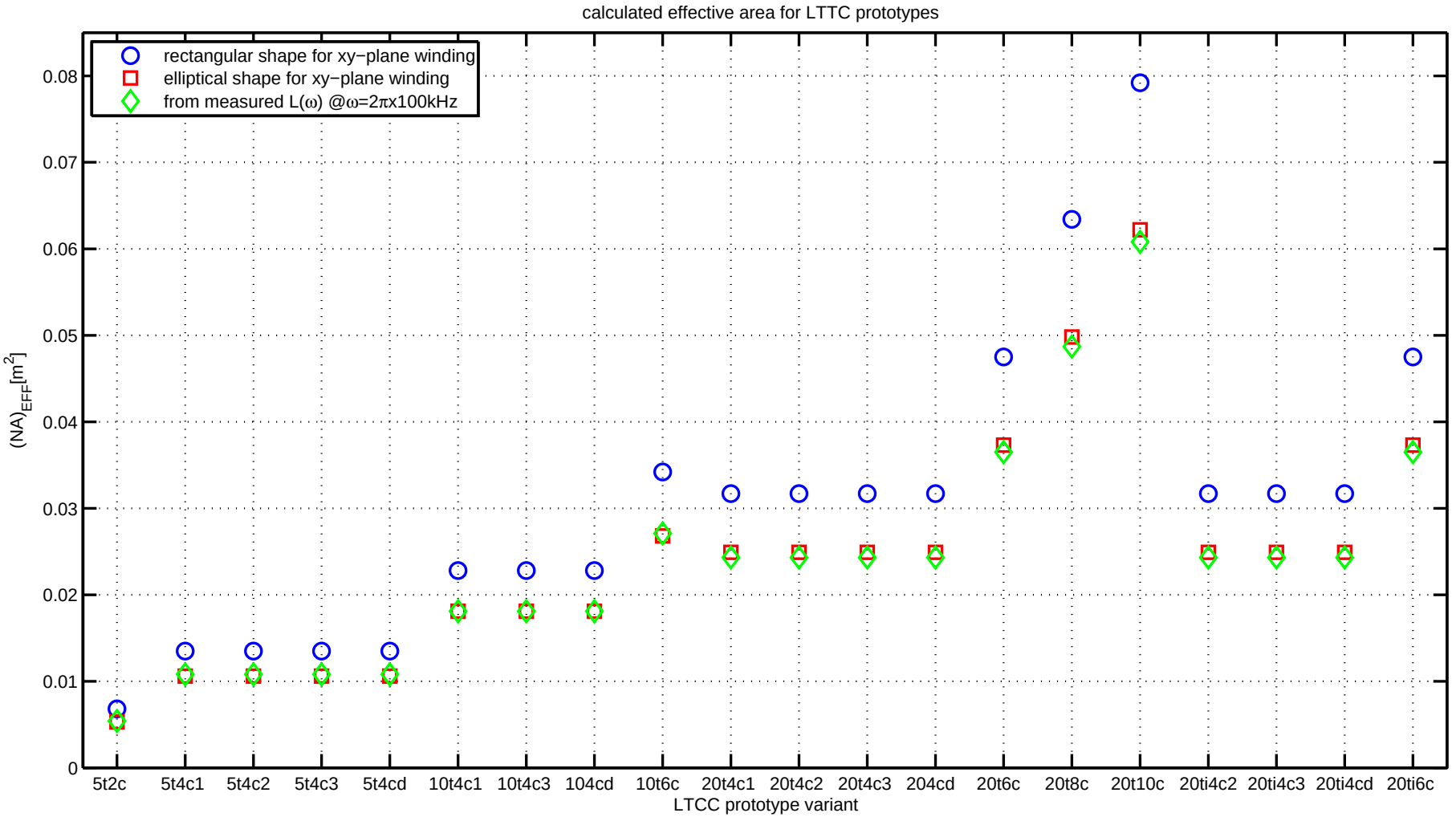

Figure9b. Calculated effective area using the rectangular and elliptical approximation for the winding shape in the xy-plane (as defined in fig8), and as obtained from the impedance measurements at 100kHz, for all the prototypes for which the impedance data are shown in fig7.

D.Testa, Figure9b, MS-356709-V4

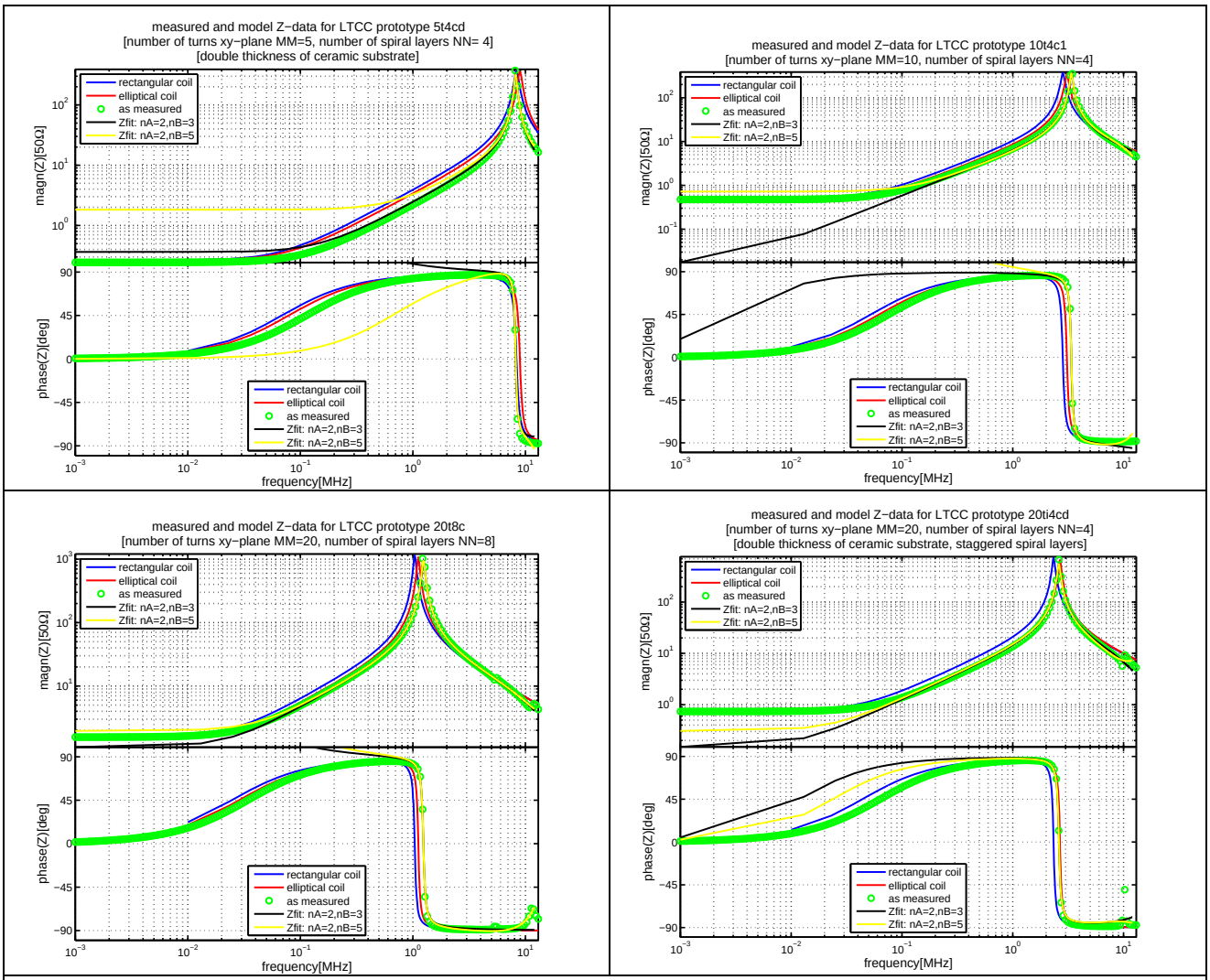

Figure10(a-d). Comparison between the measured and calculated Z-data for some of the *as-built* prototypes for the LTCC HF magnetic sensors for ITER: 5turns/4layers/double-thickness (fig10a, top left, label: 5t4cd as in fig7), 10turns/4layers (fig10b, top right, label: 10t4c1), 20turns/8layers (fig10c, bottom left, label: 20t8c) and 20turns/4layers-staggered/double-thickness (fig10d, bottom right, label: 20ti4cd), respectively. For all these prototypes we have used a DuPont951 ceramic substrate, with unfired thickness =220μm, relative dielectric constant and magnetic permeability ε_r=7.8 and μ_r=1, respectively; the metallic ink is silver, and the wire dimensions are =200×10μm (width in the xy-plane times thickness); the separation between two adjacent tracks on the xy-plane is =400μm. For clarity, all these graphs are plotted using a log10 scale for the frequency and magnitude of the Z-data, and a linear scale for the phase of the Z-data.

D.Testa, Figure10(a-d), MS-356709-V4

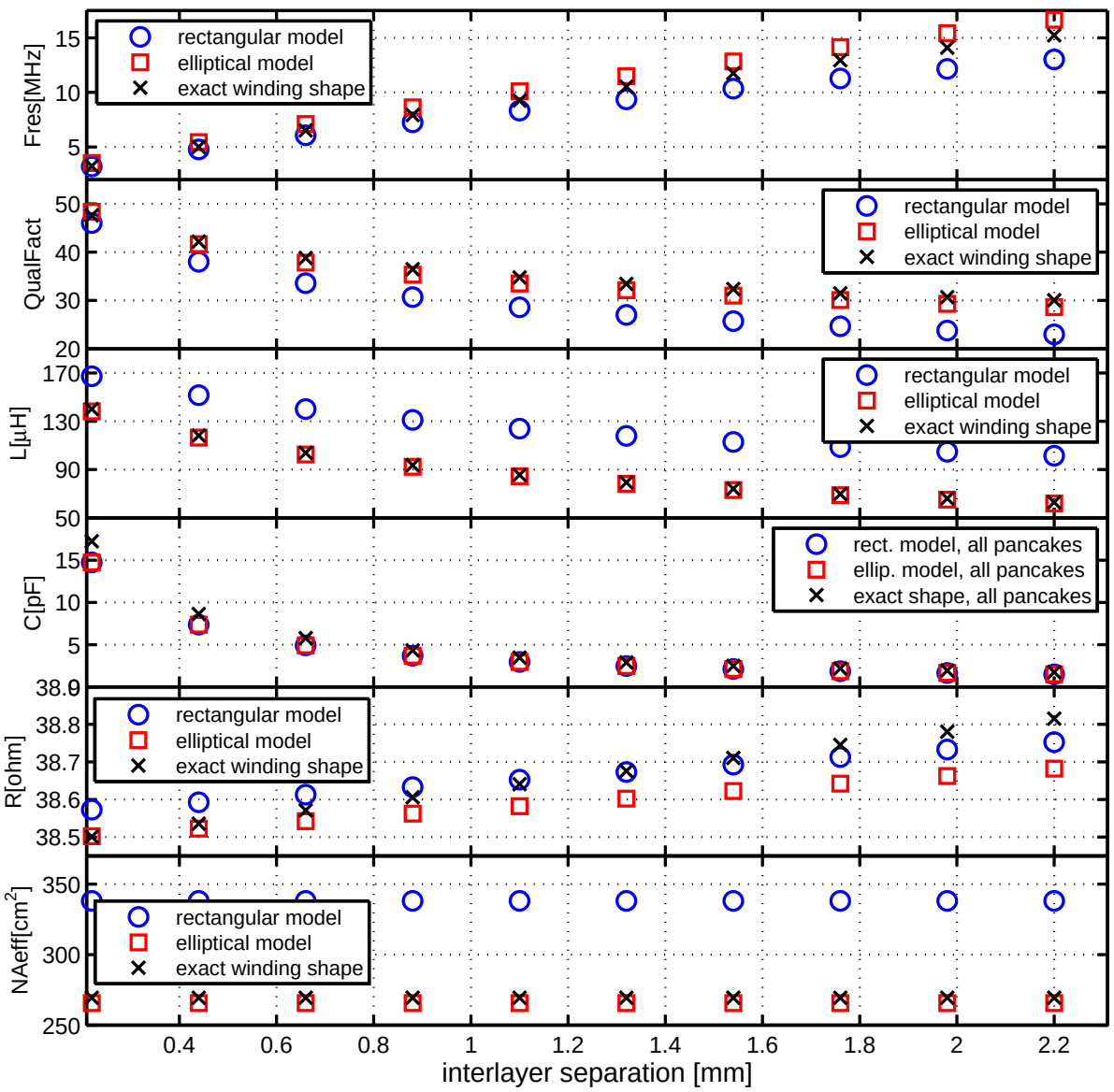

Figure11a. Scan of the main electrical parameter for an LTCC sensor as function of the inter-layer separation for a fixed number of turns (MM) in the xy-plane and number of layers (NN) along the z-axis; for this analysis we considered the rectangular, elliptical solenoid models and the exact geometry of the *as-built* design.

D.Testa, Figure11a, MS-356709-V4

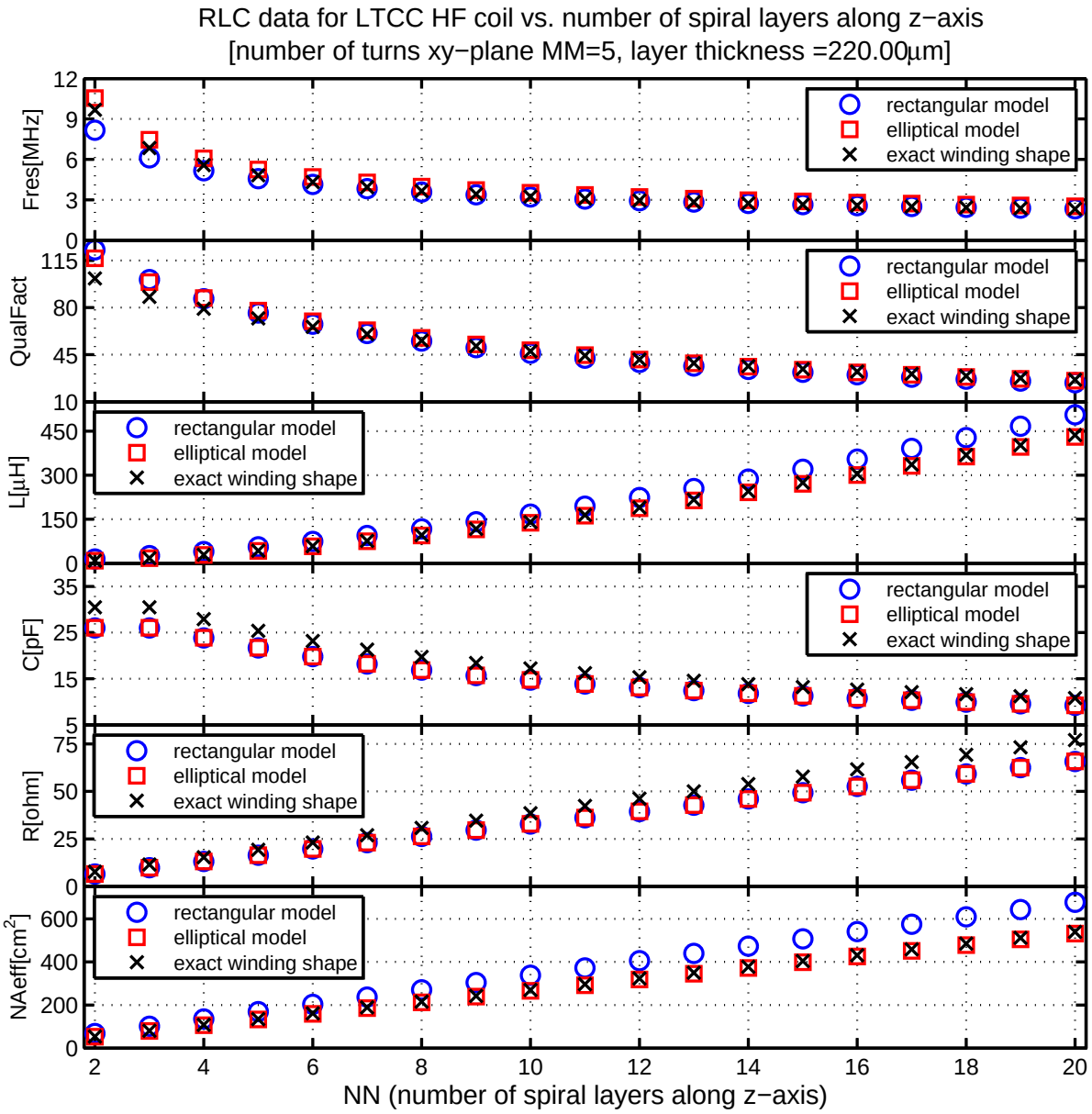

Figure11b. Scan of the main electrical parameter for an LTCC sensor as function of the number of layers (NN) along the z-axis for fixed number of turns (MM) in the xy-plane and inter-layer separation; for this analysis we considered the rectangular, elliptical solenoid models and the exact geometry of the *as-built* design.

D.Testa, Figure11b, MS-356709-V4

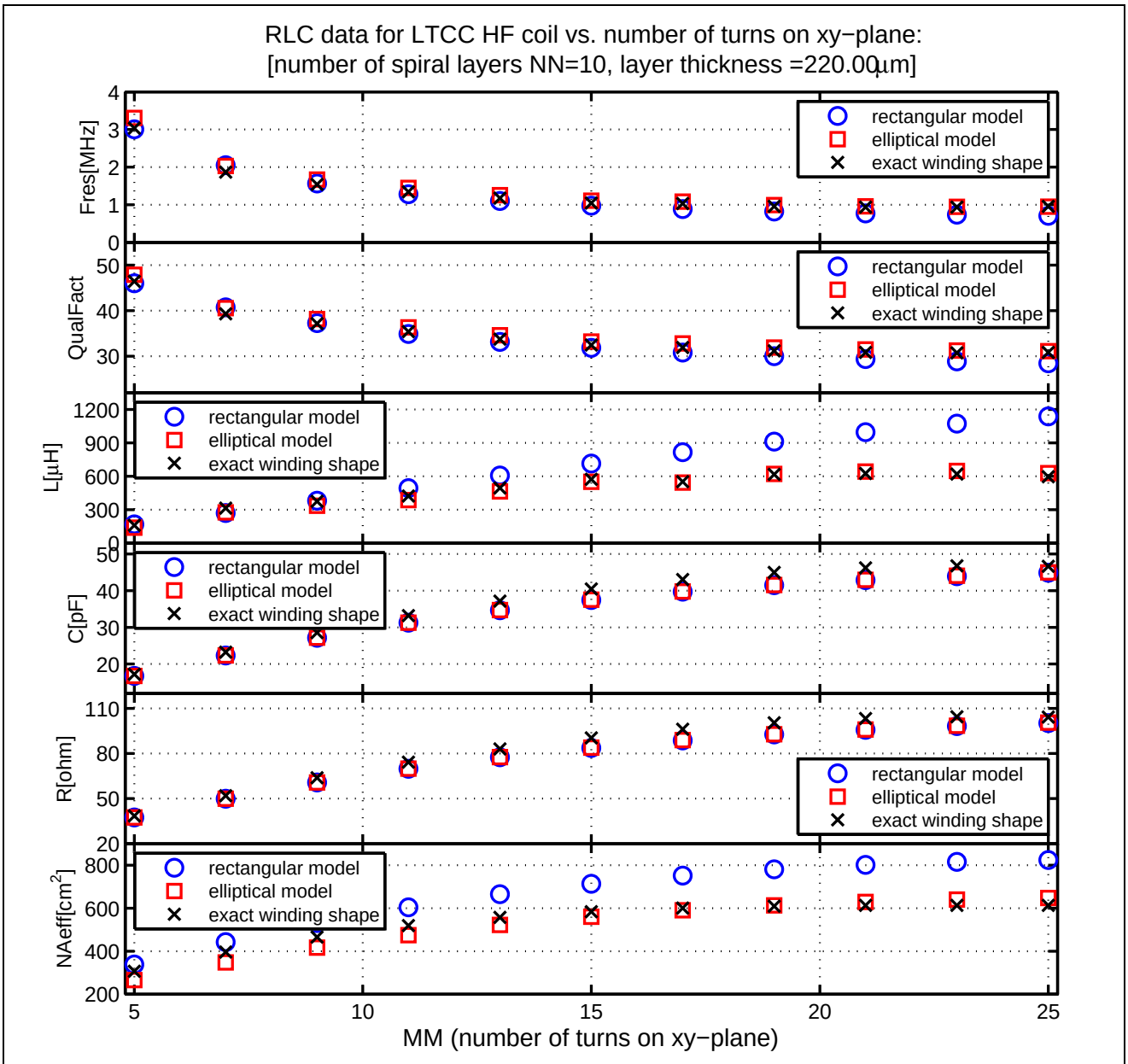

Figure11c. Scan of the main electrical parameter for an LTCC sensor as function of the number of turns (MM) in the xy-plane for a fixed number of layers (NN) along the z-axis and inter-layer separation; for this analysis we considered the rectangular, elliptical solenoid models and the exact geometry of the *as-built* design.

D.Testa, Figure11c, MS-356709-V4

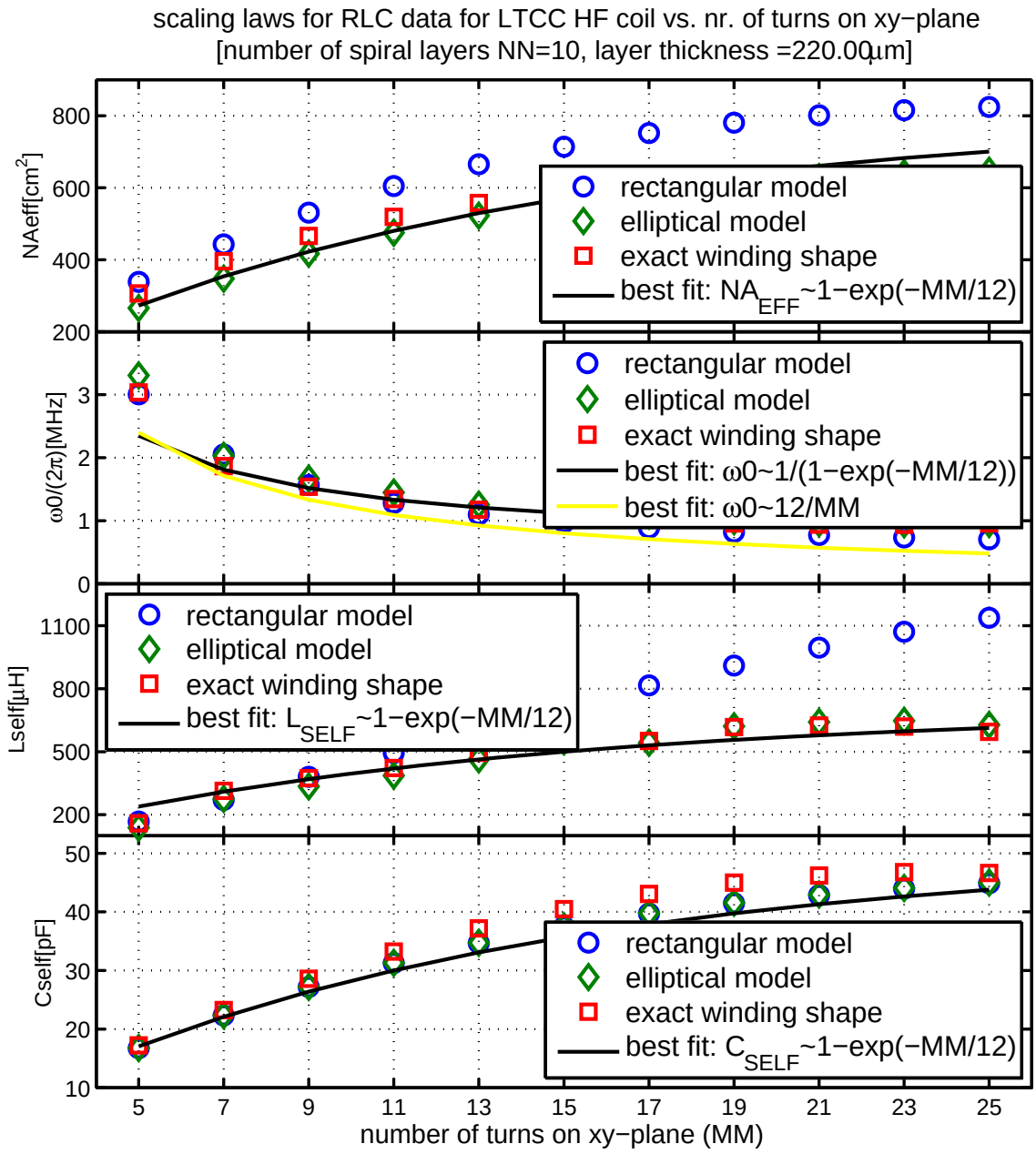

Figure12a. Calculated empirical scaling laws for the main electrical characteristics of the LTCC sensors, as function of the number of turns on the xy-plane (MM).

D.Testa, Figure12a, MS-356709-V4

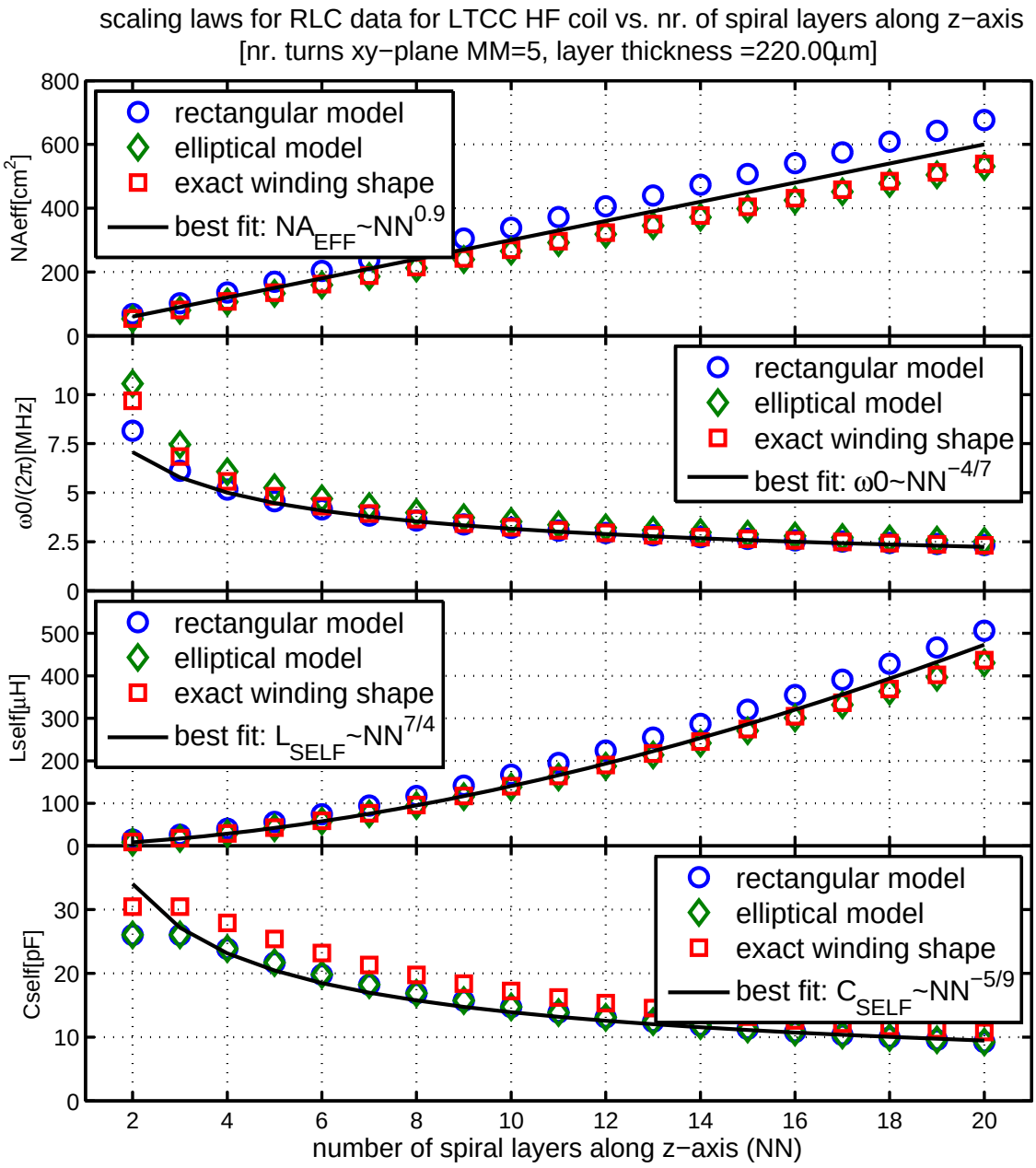

Figure12b. Calculated empirical scaling laws for the main electrical characteristics of the LTCC sensors, as function of the number of spiral layers along the z-axis (NN).

D.Testa, Figure12b, MS-356709-V4

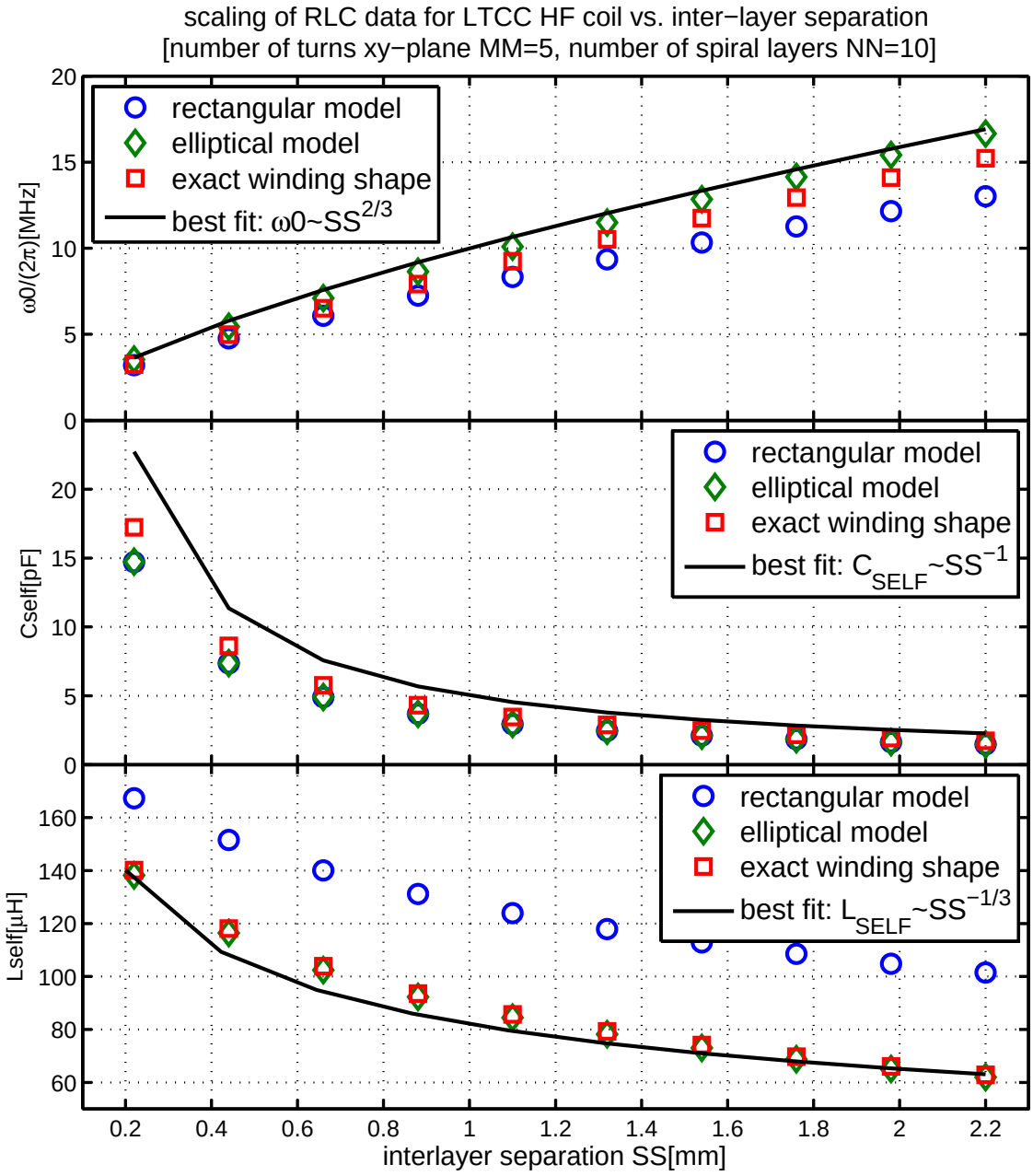

Figure12c. Calculated empirical scaling laws for the main electrical characteristics of the LTCC sensors, as function of the inter-layer separation (SS).

D.Testa, Figure12c, MS-356709-V4

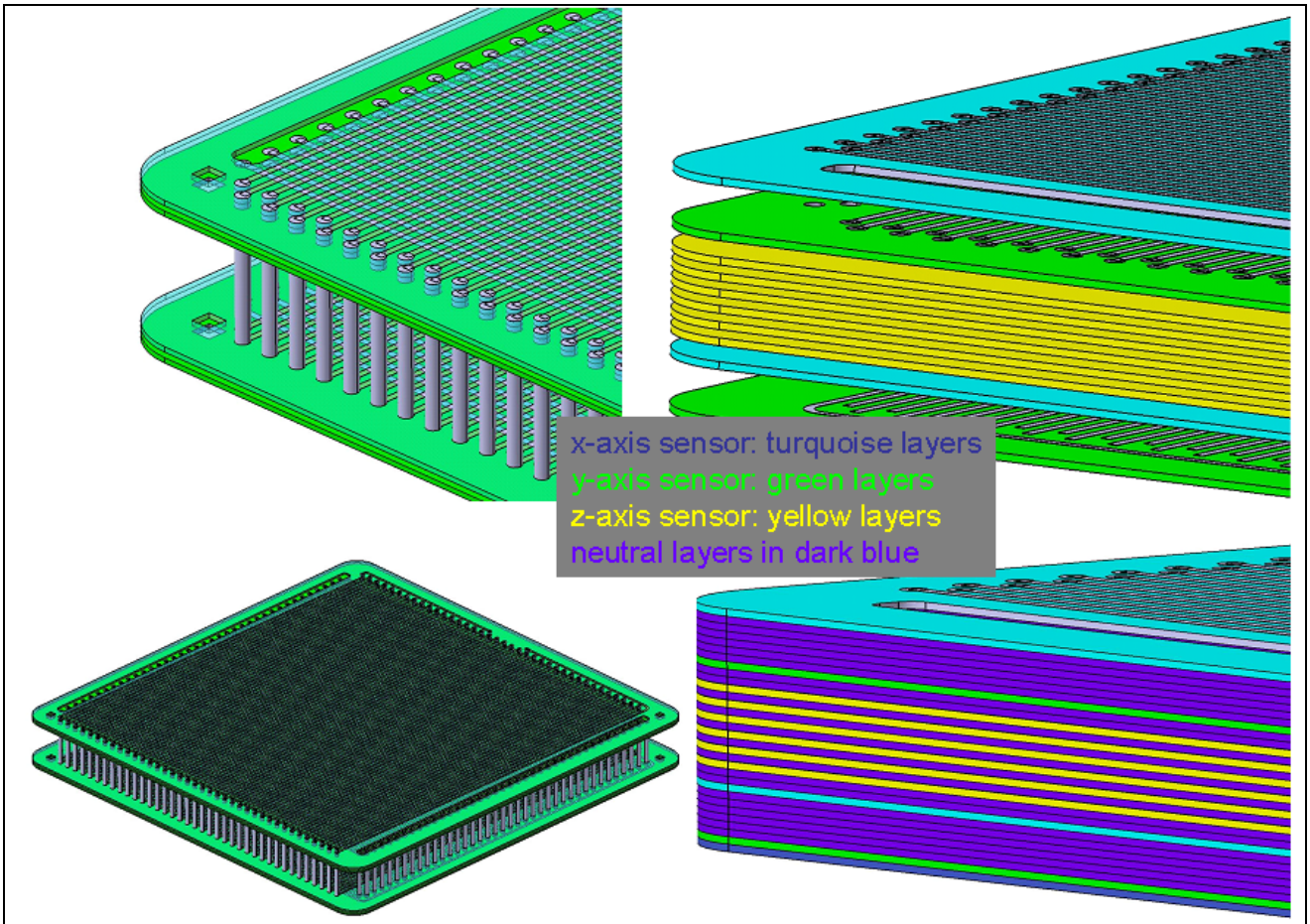

Figure13. A CAD drawing of a 3D HF magnetic sensors built upon the LTCC technology, using 10 full size DuPont951 ceramic substrates (i.e. ~600×600μm); the x- and y- measuring windings are staggered so as to separate them as much as possible (reduce stray capacitance and mutual inductance) but do still occupy ~2/3 of the device's thickness so as to have a sufficiently high effective area $(NA)_{EFF}$>0.04m^2; the z-axis measuring windings are concentrated in the central section of the device, again to decouple as much as possible the three measurement axis; note the very large number of interlaced conducting tracks and *vias*, which makes further optimization of this design essential so as to simplify the production process.

D.Testa, Figure13, MS-356709-V4

material	resistivity ρ_0 [Ωm] @300K	resistivity temperature coefficient α [K^{-1}]	thermal conductivity [$Wm^{-1}K^{-1}$] @300K	volume magnetic susceptibility χ_M [SI]
Tungsten (HTCC)	5.28×10^{-8}	0.004403	173	0.0800e-3
Molybdenum (HTCC)	5.34×10^{-8}	0.004579	138	0.1194e-3
Silver (LTCC)	1.59×10^{-8}	0.003819	429	0.0264e-3
Gold (LTCC)	2.21×10^{-8}	0.003715	318	-0.0345e-3
Palladium (LTCC)	1.08×10^{-7}	0.003875	71.8	0.8761e-3
Platinum (LTCC)	1.05×10^{-7}	0.003729	71.6	0.2965e-3
Copper (LTCC)	1.68×10^{-8}	0.003917	398	-0.0078e-3

Table1. Some of the main electrical and thermal properties of the metallic inks that can be used for magnetic sensors based on the HTCC and LTCC technologies. The temperature coefficient α increases/decreases the significant portion of the resistivity, as $\Delta\rho=\alpha\Delta T\rho_0$ where ρ_0 is the resistivity at 300K, hence $\rho(T)=\rho_0\times(1+\alpha\Delta T)$. The relative magnetic permeability μ_r of the material is defined using the volume magnetic susceptibility χ_M as $\mu_r=1+\chi_M$. Note that χ_M is a signed quantity, such that $\chi_M<0$ and $\chi_M>0$ for diamagnetic and paramagnetic materials, respectively.

D.Testa, Table1, MS-356709-V4

DuPont 951 green tape		**silver ink**	
unfired thickness	254μm±13μm	print resolution	125μm
planar shrinkage	12.7%±0.3%	coverage	60÷70cm^2/g
vertical shrinkage	15.0%±0.5%	viscosity	120÷200 @25deg
coefficient of thermal expansion (CTE)	5.8ppm/°C, from 25°C to 300°C	conductive line resistivity (fired)	2.0÷3.3 mΩ/square @6μm
specific density	3.1gr/cm^3	conductive line thickness (fired)	5÷10μm
surface roughness	<3.4μm		
thermal conductivity	3.3W/mK		
flexural strength	320MPa	**via filling**	
Young's module	120GPa	via specific density	6.2g/cm^3
dielectric constant	7.8 @3GHz	via fired resistivity	<3mΩ/square @6μm
loss tangent	0.006 @3GHz	via fill coverage	0.16cm^2/g
insulation resistance	>10^{12}Ω @100V-DC	via diameter resolution	100μm
breakdown voltage	>1kV/25μm	via fill viscosity	1500÷2800 @25deg

Table2. Physical and electrical properties of the material used for the production of the prototype LTCC HF magnetic sensors for ITER.

D.Testa, Table2, MS-356709-V4

	5t2c	5t4c1	5t4c2	5t4c3	5t4cd	10t4c1	10t4c3	104cd	10t6c	20t4c1	20t4c2	20t4c3	204cd	20t6c	20t8c	20t10c	20ti4c2	20ti4c3	20ti4cd	20ti6c
wiring length [m] rectangular shape	1.04	2.08	2.08	2.08	2.08	3.80	3.80	3.80	5.70	6.16	6.16	6.16	6.16	9.24	12.31	15.39	6.16	6.16	6.16	9.24
wiring length [m] elliptical shape	0.82	1.63	1.63	1.63	1.63	2.99	2.99	2.99	4.48	4.84	4.84	4.84	4.84	7.27	9.69	12.11	4.84	4.84	4.84	7.27
wiring length [m] manufacturing drawing	0.97	1.94	1.94	1.94	1.94	3.49	3.49	3.49	5.23	5.14	5.14	5.14	5.14	7.72	10.29	12.86	5.14	5.14	5.14	7.72
effective area [m^2] rectangular shape	0.0068	0.0135	0.0135	0.0135	0.0135	0.0228	0.0228	0.0228	0.0342	0.0317	0.0317	0.0317	0.0317	0.0475	0.0634	0.0792	0.0317	0.0317	0.0317	0.0475
effective area [m^2] elliptical shape	0.0053	0.0106	0.0106	0.0106	0.0106	0.0181	0.0181	0.0181	0.0268	0.0249	0.0249	0.0249	0.0249	0.0373	0.0498	0.0622	0.0249	0.0249	0.0249	0.0373
measured $(NA)_{EFF}$[m^2] from ωL @100kHz	0.0054	0.0108	0.0108	0.0108	0.0108	0.0181	0.0181	0.0181	0.0271	0.0243	0.0243	0.0243	0.0243	0.0365	0.0487	0.0608	0.0243	0.0243	0.0243	0.0365
R[ohm] rectangular shape	6.57	13.15	13.15	13.15	13.15	23.94	23.94	23.94	35.91	37.53	37.53	37.53	37.53	56.30	75.06	93.84	37.53	37.53	37.53	56.30
R[ohm] elliptical shape	6.58	13.16	13.16	13.16	13.16	23.96	23.96	23.96	35.95	37.60	37.60	37.60	37.60	56.40	75.20	94.00	37.60	37.60	37.60	56.40
R[ohm] measured Zdata	6.92	13.23	13.23	13.23	12.26	23.96	23.96	23.96	40.17	38.17	40.41	39.28	35.28	63.91	82.72	107.56	41.26	39.19	37.41	64.00
R[ohm]-DC measured (ohm-meter)	7.00	13.20	13.20	13.20	12.20	23.80	23.80	23.80	39.10	40.82	40.82	40.82	40.84	61.80	81.64	102.05	40.82	40.82	40.84	61.23
Lself[μH] rectangular shape	11.65	31.79	31.79	31.79	30.65	72.96	72.96	70.62	144.30	140.41	140.41	140.41	136.55	290.32	488.81	732.85	140.41	140.41	136.55	290.32
Lself[μH] elliptical shape	8.87	29.22	29.22	29.22	26.63	61.47	61.47	56.81	134.62	110.79	110.79	110.79	104.26	243.86	421.02	637.49	110.79	110.79	104.26	243.86
Lself[μH] measured Zdata	6.72	24.68	23.85	24.69	22.15	67.44	70.27	62.99	149.19	136.67	136.59	137.10	124.56	300.74	518.54	759.94	136.19	138.74	129.49	298.03
Cself[pF] rectangular shape	26.01	23.84	23.84	23.84	11.92	43.41	43.41	21.70	36.04	68.05	68.05	68.05	34.03	56.51	48.12	42.00	68.05	68.05	34.03	56.51
Cself[pF] elliptical shape	26.03	23.86	23.86	23.86	11.93	43.45	43.45	21.73	36.08	68.17	68.17	68.17	34.09	56.61	48.21	42.08	68.17	68.17	34.09	56.61

Cself[pF] measured Zdata	22.29	20.81	21.53	20.80	17.45	31.53	30.26	23.11	27.66	44.11	44.13	43.97	30.14	35.39	32.96	29.88	44.26	41.49	28.99	35.71
ratio Cself (pancakes) 1st neighbors vs. all	1.00	0.36	0.36	0.36	0.36	0.36	0.36	0.36	0.26	0.36	0.36	0.36	0.36	0.26	0.22	0.20	0.36	0.36	0.36	0.26
FreqRes[MHz] rectangular shape	9.14	5.78	5.78	5.78	8.33	2.83	2.83	4.07	2.21	1.63	1.63	1.63	2.33	1.24	1.04	0.91	1.63	1.63	2.33	1.24
FreqRes[MHz] elliptical shape	12.83	6.03	6.03	6.03	8.98	3.06	3.06	4.53	2.28	1.83	1.83	1.83	2.67	1.35	1.21	0.97	1.83	1.83	2.67	1.35
FreqRes[MHz] measured Zdata	*13.00*	7.02	7.02	7.02	8.10	3.45	3.45	4.17	2.48	2.05	2.05	2.05	2.60	1.54	1.22	1.06	2.05	2.10	2.60	1.54
bandwidth[kHz] rectangular shape	1243.32	1045.69	1045.69	1045.69	2311.66	624.82	1791.74	860.63	401.89	280.60	243.86	243.86	401.92	203.15	180.68	159.25	280.60	280.60	401.92	185.45
bandwidth[kHz] elliptical shape	1331.33	1063.34	1063.34	1063.34	2342.37	655.20	2150.47	901.33	410.69	316.36	279.69	279.69	444.34	221.63	193.02	168.78	316.37	316.37	444.34	203.97
bandwidth[kHz] measured Zdata	1635.87	1229.39	1215.30	1231.88	1709.23	811.97	833.63	831.14	469.15	366.36	317.86	313.84	440.25	275.81	231.48	204.64	377.40	382.28	454.90	247.40
quality factor rectangular shape	46.20	34.74	34.74	34.74	22.63	28.44	28.44	29.68	34.50	36.46	41.95	41.95	36.50	38.43	36.09	35.79	36.46	36.46	36.50	42.10
quality factor elliptical shape	49.43	35.62	35.62	35.62	23.98	29.53	29.53	31.58	34.94	36.37	41.14	41.14	37.77	38.40	36.37	36.17	36.37	36.37	37.75	41.73
quality factor measured Zdata	49.96	35.90	36.32	35.82	29.76	26.70	26.02	31.54	31.38	35.16	40.52	41.04	37.08	35.14	33.04	32.42	34.12	34.48	35.92	39.18

Table3. Measured and calculated [R, L, C] data for the different LTCC prototypes; the same code-naming as in fig7 is used in this table; the entry "measured $(NA)_{EFF}$ [m^2] from ωL @100kHz" is obtained from solving the Ampère's law for the sensor, as described in Section-III.

D.Testa, Table3, MS-356709-V4